

ORNL/SPR-2023/2925
CRADA/NFE-21-08609

Prediction of the influence of strain magnitude and strain path on the resulting microstructure and post-forming mechanical behavior of RA containing high formability steels



Xiaohua Hu
Jiahao Cheng
Brian Lin
Sriram Sadagopan
Narayan S. Pottore
Hong Zhu

07/31/2023

DOCUMENT AVAILABILITY

Reports produced after January 1, 1996, are generally available free via US Department of Energy (DOE) SciTech Connect.

Website <http://www.osti.gov/scitech/>

Reports produced before January 1, 1996, may be purchased by members of the public from the following source:

National Technical Information Service
5285 Port Royal Road
Springfield, VA 22161
Telephone 703-605-6000 (1-800-553-6847)
TDD 703-487-4639
Fax 703-605-6900
E-mail info@ntis.gov
Website <http://www.ntis.gov/help/ordermethods.aspx>

Reports are available to DOE employees, DOE contractors, Energy Technology Data Exchange representatives, and International Nuclear Information System representatives from the following source:

Office of Scientific and Technical Information
PO Box 62
Oak Ridge, TN 37831
Telephone 865-576-8401
Fax 865-576-5728
E-mail reports@osti.gov
Website <http://www.osti.gov/contact.html>

This report was prepared as an account of work sponsored by an agency of the United States Government. Neither the United States Government nor any agency thereof, nor any of their employees, makes any warranty, express or implied, or assumes any legal liability or responsibility for the accuracy, completeness, or usefulness of any information, apparatus, product, or process disclosed, or represents that its use would not infringe privately owned rights. Reference herein to any specific commercial product, process, or service by trade name, trademark, manufacturer, or otherwise, does not necessarily constitute or imply its endorsement, recommendation, or favoring by the United States Government or any agency thereof. The views and opinions of authors expressed herein do not necessarily state or reflect those of the United States Government or any agency thereof.

Division or Program Name

Prediction of the influence of strain magnitude and strain path on the resulting microstructure and post-forming mechanical behavior of RA containing high formability steels

Xiaohua Hu
Jiahao Cheng
Brian Lin (ArcelorMittal)
Sriram Sadagopan(ArcelorMittal)
Narayan S. Pottore(ArcelorMittal)
Hong Zhu (ArcelorMittal)

Date Published:

Prepared by
OAK RIDGE NATIONAL LABORATORY
Oak Ridge, Tennessee 37831-6283
managed by
UT-BATTELLE, LLC
for the
US DEPARTMENT OF ENERGY
under contract DE-AC05-00OR22725

1. Abstract

In third generation advanced high strength steels (AHSS) there is considerable potential to alter the transformation characteristics through variation of process parameters and through changes in chemical composition. This proposal aims to utilize this known phenomenon to develop microstructure-based transformation models to predict austenite stability as a function of chemical composition, strain level, deformation mode. The ultimate intent is to predict microstructure and performance during room temperature forming to produce automotive structural components with superior strength and failure resistance, ...

2. Statement of Objectives

High formability (HF) steels are part of the 3rd-generation of Advanced High Strength Steels (3rd Gen AHSS) with a unique combination of high strength-high ductility which is being developed by ArcelorMittal USA Research LLC (Participant). Detailed understanding of the forming behavior of these evolving HF steels and the resulting changes in microstructure will significantly enhance the successful implementation of these products in the automotive industry. Lowering the weight of vehicles helps in increasing fuel efficiency and provide environmental benefits by reducing the Carbon footprint. HF steels also have a significant cost advantage over the previous generation of AHSS such as stainless and TWIP steels, especially during part manufacturing and vehicle assembly, where because of the chemical composition in these steels, they are easier to be welded using the current automotive infrastructure. These steels therefore have a higher potential to be used in vehicles without new investment. Furthermore, the material that is planned for use in this study are industrially produced, building on the attainment of the past DOE ICME project.

The current High-Performance Computing for Energy Innovation (HPC4EI) proposal seeks to develop predictive models to enhance the development of industrial 3rd Gen. steels for automotive components by controlling the deformation-induced martensite formation to achieve high strength and vehicle weight reduction. HPC4EI support to develop microstructural mechanism-based modeling methodology to predict austenite stability will be essential for advancing the state of the art and shorten the time to develop optimized steel grades. This proposal fits well with the stated aims of the HPC4EI to improve energy efficiency and accelerate innovative new processes through the use of high-performance computing (HPC). Participant is well recognized as an Industry leader in production of 3rd gen. AHSS.

HPC4EI computational modeling will be able to predict quantitatively the amount of austenite transformed in the HF steels in different deformation modes. The primary use of this information at Participant will be to predict microstructure and performance during room temperature forming process to produce automotive structural components with superior strength by controlling deformation and failure resistance. A secondary use of the HPC4EI austenite stability computations based on using thermodynamic considerations is the possibility of developing relationships between chemical composition and austenite stability that could be very useful for developing new HF grades at Participant.

3. Benefits to the Funding DOE Office's Mission

This project will benefit the U.S. Department of Energy Advanced Materials & Manufacturing Technology office mission of developing light-weight materials for in-service energy saving of high way vehicles.

4. Technical Discussion of the Work Performed by All Parties

In order to most effectively and efficiently meet the project objectives outlined above, the team established a project plan with five tasks

- 1) Alloy selection, data collection, transformation energy and austenite stacking fault energy (SFE) calculations.
- 2) Crystal plasticity (CP) material model development of multi-phase material with consideration of martensitic transformation.
- 3) Constitutive parameters determination by integrated in-situ neutron diffraction and crystal plasticity modeling.
- 4) Conduct large sets of crystal plasticity modeling using HPC and validation to predict austenite transformation kinetics in different deformation modes for the two selected grades.
- 5) Build RO-SVM for component level simulation and process parameter optimization.

4.1 Alloy selection, data collection, transformation energy and austenite stacking fault energy (SFE) calculations

The investigated material is ArcelorMittal's GI Fortiform® grade high formability quenching and partitioning steels QP980. The microstructure primarily comprises of retained austenite (γ), ferrite (α), bainite, and martensite (α') phases. The scanning electron microscopy (SEM) and electron backscatter diffraction (EBSD) characterization were conducted on the as-received samples in rolling (RD), transverse (ND) and normal direction (ND) and shown in Figure 1 and 2, respectively. The EBSD scans, performed with a resolution of 0.1 μ m stepping size, identified approximately 9.8 vol% isolated RA island, referred to as bulk RA (γ_B) and are illustrated in Figure 3a. Conversely, the film RA (γ_F), with a thickness of less than 100nm, resides amongst the fine martensite laths and is not discernible with EBSD due to its small size. The x-ray diffraction of the same batch samples showed an average RA volume fraction of ~16.2 vol%, indicating there are ~6.4 vol% film austenite and small bulk austenite not detected by EBSD in the sample. The pole figures of BCC ferrite and BCT martensite phases, as well as the pole figures of the FCC retained austenite phase are calculated from the EBSD and shown in Figure 3b.

The ferrite and martensite can be differentiated based on the quality of their diffraction patterns [1,2] due to the fact that martensite has a more distorted body-centered tetragonal (BCT) structure that has a unit cell with anisotropic carbon distribution and differs from the body-centered-cubic (BCC) α -ferrite phase. Moreover, during the "partitioning" step, a reduction in the carbon content within the martensite matrix occurs, leading to a modification of the lattice parameter and aligning the BCT structure of the martensite closer to the cubic structure of the ferrite phase. This process, in turn, results in the formation of a softer tempered martensite compared to the as-transformed fresh martensite. In the as-received material, the fresh martensite comprises only a small volume fraction. Figure 4b marks the ferrite (~39.7 vol%), tempered

martensite (~42.6 vol%) and fresh martensite (~7.9vol%) phases in the EBSD image, identified based on the relative diffraction pattern quality index.

For each phase, the grain dimensions are measured and listed in table 1. The ferrite grains are mostly in a “pancake” shape, while the (individual) martensite and austenite grains are relatively equiaxed and about 4-5 times smaller than ferrite grains.

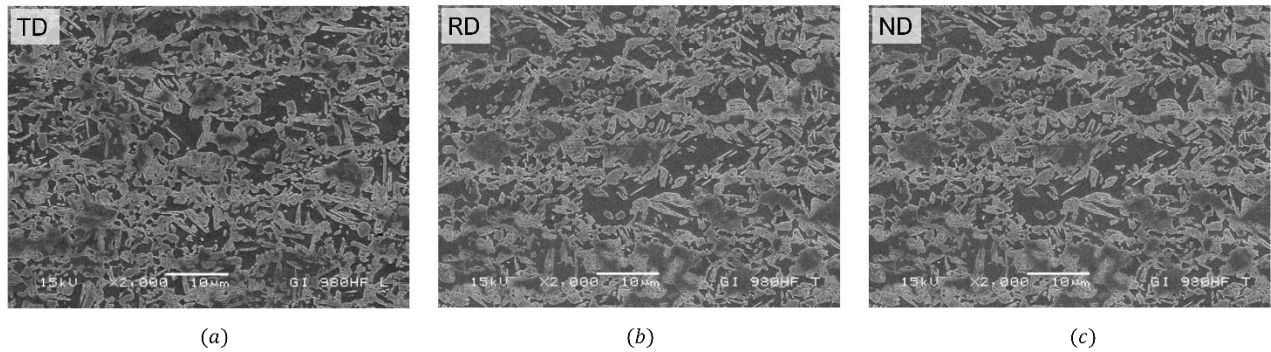


Fig. 1. The SEM scan images of the as-received GI Fortiform® QP 980 steel sample.

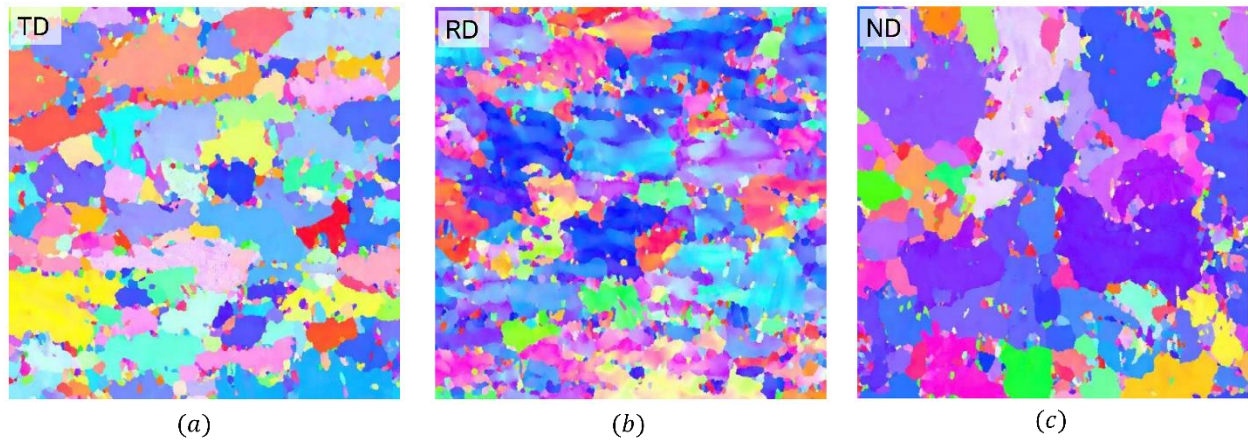


Fig. 2. The EBSD scan images of the as-received GI Fortiform® QP 980 steel sample.

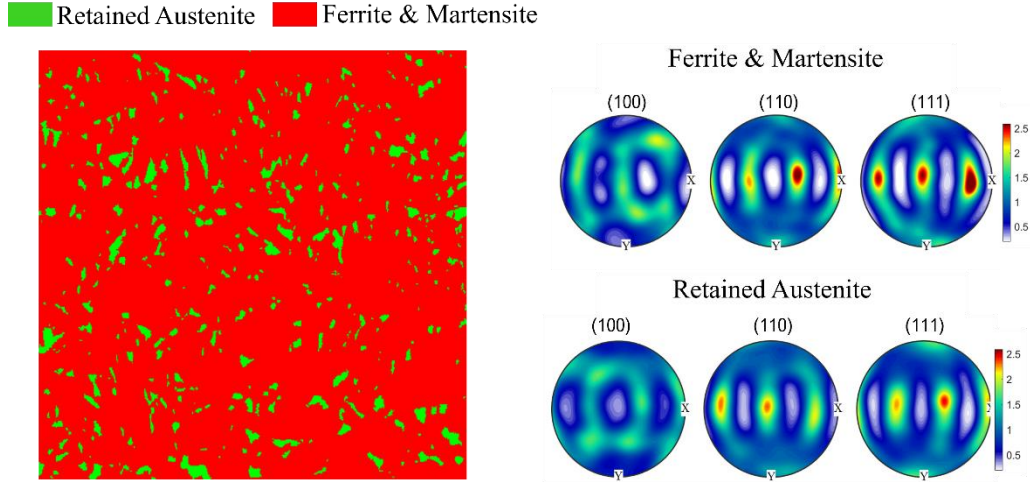


Fig. 3. (a) The bulk retained austenite (γ_B) phases identified from EBSD scans, and (b) the respective pole figures of bulk retained austenite phase and rest ferrite & martensite phases.

Table 1: Measured grain size (via intercept length) (unit: μm)

| phase | RD | | TD | | ND | |
|------------|--------|-------|--------|-------|--------|-------|
| | Horiz. | Vert. | Horiz. | Vert. | Horiz. | Vert. |
| Ferrite | 2.357 | 1.754 | 2.322 | 1.919 | 2.731 | 2.875 |
| Martensite | 0.548 | 0.458 | 0.444 | 0.456 | 0.479 | 0.467 |
| Austenite | 0.323 | 0.357 | 0.433 | 0.365 | 0.409 | 0.371 |

It is crucial to account for the film austenite that is not detected by EBSD, which makes up approximately 6.4 vol% of the sample. In this work, the film austenite phase is presumed to be uniformly distributed within the tempered martensite phase, meaning each tempered martensite element is assumed to contain a sub-portion of film austenite. An iso-strain homogenization approach (e.g., [3]) is utilized to model the mechanical response of the combined $\alpha'_T + \gamma_F$ structure, as detailed in section 3.4. The crystal orientation of the film austenite grains cannot be obtained from EBSD. Instead, it is acquired through the utilization of the MTEX martensite parent grain reconstruction toolbox ([4,5]) applied to the EBSD data, a process demonstrated in Figure 5.

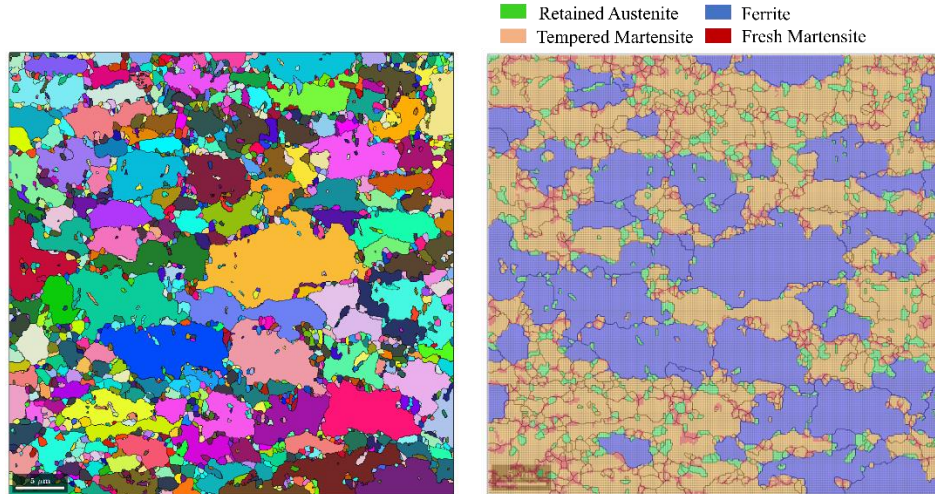


Fig. 4. (a) The bulk retained austenite (γ_B) phases identified from EBSD scans, and (b) the respective pole figures of bulk retained austenite phase and rest ferrite & martensite phases.

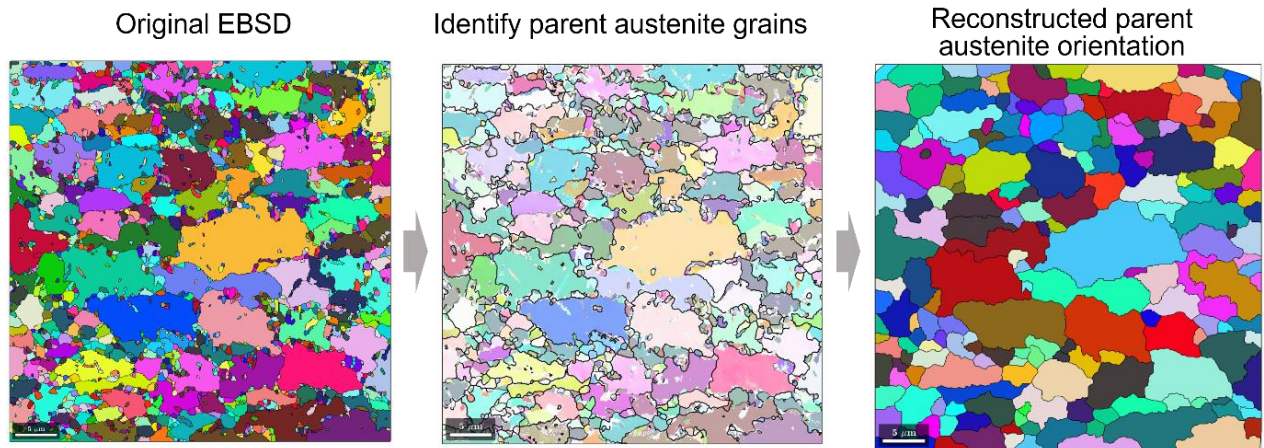


Fig. 5. Reconstruction of parent austenite grain for determining the orientation of film austenite in the martensite matrix.

4.2 Crystal plasticity (CP) material model development of multi-phase material with consideration of martensitic transformation

In this crystal plasticity FE model, the following phases are considered: ferrite (α), tempered martensite (α'_T), fresh martensite (α'_N), bulk retained austenite (γ_B) and film retained austenite (γ_f), while the bainite phase is also treated as tempered martensite phase for simplicity. The FE model is obtained by conversion of the EBSD image in Figure 4 into a 2D FE mesh, where the phase and crystallographic orientation of each element is directly assigned from the EBSD map. Note that because the film retained austenite is thinner than EBSD scanning resolution, it is assumed distributed in the tempered martensite and modeled

with an iso-strain assumption based homogenized method. The constitutive formulation for each phase is described as follows.

4.2.1 general crystal plasticity equations for BCC or BCT crystal

The constitutive behavior of α -ferrite (BCC) or martensite (BCT) crystals, including both tempered martensite and pre-existing fresh martensite, is modeled using a power-law rate-dependent crystal plasticity model (see [6] for details) but different material parameters, which is summarized as the following:

$$\text{Kinematic equation: } \mathbf{L} = \dot{\mathbf{F}}\mathbf{F}^{-1}; \mathbf{L} = \dot{\mathbf{F}}\mathbf{F}^{-1} = \mathbf{L}^e + \mathbf{L}^{slip}; \quad (1)$$

$$\text{Elastic – plastic decomposition: } \mathbf{F} = \mathbf{F}^e \mathbf{F}^{slip}; \mathbf{L}^e = \dot{\mathbf{F}}^e \mathbf{F}^{e-1}; \mathbf{L}^{slip} = \mathbf{F}^e \dot{\mathbf{F}}^p \mathbf{F}^{p-1} \mathbf{F}^{e-1} \quad (2)$$

$$\text{Crystal plasticity Flow rule: } \mathbf{L}^{slip} = \dot{\mathbf{F}}^{slip} \mathbf{F}^{slip-1} = \sum_i^{Nslip_{BCC}} \dot{\gamma}^i \mathbf{m}^i \otimes \mathbf{n}^i \quad (3)$$

$$\text{Slip rate equation: } \dot{\gamma}_\alpha^i = \dot{\gamma}_0 \left| \frac{\tau^i}{g^i} \right|^{\frac{1}{m}} \text{sign}(\tau^i) \quad (4)$$

$$\text{Voce – type hardening law: } g^i = g_0^i + (g_s^i + \theta_1^i \gamma) \left[1 - \exp\left(-\frac{\theta_0^i \gamma}{g_s^i}\right) \right] \quad (5)$$

$$\text{Stress – strain relation: } \boldsymbol{\sigma} = \frac{1}{\det(\mathbf{F})} \mathbf{F} \mathbf{S} \mathbf{F}^T \text{ and } \mathbf{S} = \mathbb{C}^e : \frac{1}{2} (\mathbf{F}^e \mathbf{F}^{eT} - \mathbf{I}) \quad (6)$$

Here, \mathbf{F} , \mathbf{F}^e and \mathbf{F}^{slip} are the total, elastic and slip-induced plastic deformation gradient tensors, respectively, which have a multiplicative relation: $\mathbf{F} = \mathbf{F}^e \mathbf{F}^{slip}$. \mathbf{L}^{slip} is the plastic velocity gradient tensor due to slip. $\boldsymbol{\sigma}$ and \mathbf{S} are the Cauchy and 2nd Piola-Kirchhoff stress tensors, respectively, and \mathbb{C}^e is the elastic stiffness tensor. $\dot{\gamma}^i$, \mathbf{m}^i and \mathbf{n}^i are the slip rate, slip direction vector and slip plane normal vector, respectively. $\dot{\gamma}_0$ is the reference slip rate, m is the strain rate sensitivity, and γ is the accumulated slip on all slip systems, i.e. $\gamma = \sum_i^{Nslip} \int_0^t |\dot{\gamma}^i| dt$. g^i , g_0^i , g_s^i are the total, initial and saturation slip system resistances, respectively. χ^α is the back stress on the α -th slip system. θ_1^i , θ_0^i . The variables g^i , g_0^i , g_s^i are the total, initial and saturation slip system resistances, respectively. χ^α is the back stress on the α -th slip system. θ_1^i , θ_0^i . In this work, 24 slip systems (12 {110} <111> systems and 12 {112} <111> systems) are assumed for BCC and BCT crystals. For ease of modeling, the BCT martensite phase is approximated to have the same slip systems as BCC crystal. The ferrite, tempered martensite and fresh martensite phases have different values of material yield and hardening parameters in equation (1-6), which are calibrated by fitting the HEXRD-measured lattice strain and are depicted in section 4.1.

4.2.2 Transformation model for bulk retained austenite

The transformation model for the transition from austenite to fresh martensite is comprehensive and can be delineated by four key components: (1) a transformation initiation criterion, (2) the transformation-induced deformation, (3) the variant selection criterion, and (4) the transition from FCC to BCT crystal structure. Each of these components will be elaborated in detail within this section.

4.2.2.1 martensitic transformation criterion

A stress-assisted martensitic transformation [7–9] model is adopted for determining the critical moment of transformation initiation. The transformation theory assumes martensitic transformation is triggered when the total Gibbs free energy change, including a chemical energy term (ΔG_{chem}) and mechanical work (ΔG_{mech}) for transformation, equals to or exceeds a critical energy value, which is expressed as [7,9]:

$$\Delta G_{chem} + \Delta G_{mech} = \Delta G_{crit} \Leftrightarrow \gamma \rightarrow \alpha' \quad (7)$$

here, the chemical “driving force” ΔG_{chem} is the free energy change accompanying the transformation from austenite (γ) to the ferrite of the same chemical composition:

$$\Delta G_{chem}(X_i, T) = G_\alpha - G_\gamma + \Delta f^* \quad (8)$$

where G_α and G_γ are the free energies of the RA phase and supersaturated ferrite phase, respectively at a given temperature T and chemical composition X_i , which can be calculated by using ThermoCalc® database [7,10]. Δf^* is the Zener ordering term for BCC-ferrite into BCT-martensite. The mechanical driving force is the external mechanical work due to the interaction of the applied stress field σ and the transformation volume change. The Olson-Tsuzaki-Cohen model [11] proposed an empirical expression of ΔG_{mech} with dependence on stress state, which is written as [9]:

$$\Delta G_{mech}(\sigma) = \sigma \left(\frac{\partial \Delta G_{Mech}}{\partial \sigma} \right) = -c_1 \sigma_{vm} - c_2 \left(\frac{\Delta V}{V} \right) \sigma_H + c_3 (1 - \exp(c_4 * \sigma_{vm})) \quad (9)$$

where σ_{vm} is the von-Mises stress, σ_H is the hydrostatic stress for tension or compression stress-state dependence, $\frac{\Delta V}{V} = 0.04$ is the fractional volume change upon transformation, and $c_{1...4}$ are fitting parameters.

The term ΔG_{crit} term in equation (7) is the critical energy barrier for transformation, which can be physically interpolated as the sum of the transformation-associated elastic strain energy, the austenite/martensite interfacial energy, the frictional work of interfacial motion due to solid solution and the frictional work due to forest dislocation [7]. As this work focuses on the deformation of QP980 at room temperature, we treat ΔG_{chem} as constant and further define an effective critical transformation energy $\Delta G_{crit}^{eff} = \Delta G_{crit} - \Delta G_{chem}$, which is calibrated from the transformation rate measured in HEXRD

experiment. The bulk RA and film RA have different carbon content and transformation stability[12], therefore should use separate values of effective critical transformation energy ΔG_{crit}^{eff} in the model.

4.2.2.2 transformation-induced deformation

The martensitic transformation causes a displacive lattice deformation and results in changing of the lattice from austenite FCC structure to martensite BCT structure with a new crystallographic orientation. There are several theories to formulate the mechanical deformation induced by austenite-to-martensite transformation, such as Wechsler–Lieberman–Read (WLR) theory [13,14], elastic-strain-energy minimization theory [14], and etc. In this work, a phenomenological transformation theory, proposed by Ball and James[15], Hane and Shield[16], and implemented in CPFE model in [17–20], is adopted and verified with the HEXRD experiment. This theory assumes the transformation forms a plate-shape martensite region inside the parent austenite grain and locally induces a jump in strain between the transformed fresh martensite region and the austenite matrix. In the finite deformation framework, the kinematic behavior of austenite incorporating transformation-induced deformation can be described by a three-terms multiplicative deformation gradient tensor, expressed as:

$$\mathbf{F} = \mathbf{F}^e \mathbf{F}^{slip} \mathbf{F}^{tr} \quad (10)$$

where \mathbf{F}^{tr} is the local deformation inside the martensite induced by the transformation and is expressed as:

$$\mathbf{F}^{tr} = \mathbf{I} + \llbracket \mathbf{F}^{tr} \rrbracket; \quad \llbracket \mathbf{F}^{tr} \rrbracket = \mathbf{F}^{\alpha'_N} - \mathbf{F}^\gamma = \mathbf{R}^{tr} \mathbf{U}^{tr} - \mathbf{I} \quad (11)$$

here $\llbracket \mathbf{F}^{tr} \rrbracket$ denotes the strain jump between the transformed martensite region ($\mathbf{F}^{\alpha'_N}$) and parent austenite matrix (\mathbf{F}^γ), assuming no further slip or elastic stretch. \mathbf{U}^{tr} is the Bain deformation tensor (transformation stretch tensor) as a function of the lattice parameters of austenite and martensite lattices, and \mathbf{R}^{tr} is the rotation tensor to account for the orientation relationship for the parent austenite and transformed martensite lattices so that their respect close-packing plane and directions are roughly parallel[18]. In general, for the transformation from austenite to a single martensite variant, \mathbf{U}^{tr} can be expressed in the RA cubic material reference basis¹ as [17,21]:

¹Note that there are four orthogonal coordinate systems (basis) used in this model, namely the sample basis (\mathbf{e}_i), single grain basis (\mathbf{e}_i^g), RA material reference basis (\mathbf{e}_i^r), and martensite material reference basis (\mathbf{e}_i^m). The sample basis refers to the global coordinates with respect to the test sample setup, e.g., \mathbf{e}_1 - \mathbf{e}_2 - \mathbf{e}_3 axes aligned with loading direction (LD), transverse direction (TD), sample thickness direction (STD). The RA cubic material reference basis refers to the coordinates defined with austenite FCC lattice axes, e.g., \mathbf{e}_1 - \mathbf{e}_2 - \mathbf{e}_3 axes aligned with $[100]_\gamma$, $[010]_\gamma$ and $[001]_\gamma$. The single grain basis is identical to austenite cubic material reference but is more generally used to define the coordinates after the austenite-to-martensite transformation. The martensite cubic material reference basis refers to the coordinates defined with respect to the martensite BCT lattice axes, e.g., \mathbf{e}_1 - \mathbf{e}_2 - \mathbf{e}_3 axes aligned with

$$\mathbf{U}^{tr} = \frac{\sqrt{2}a^M}{a^A} \mathbf{I} + \left(\frac{c^M}{a^A} - \frac{\sqrt{2}a^M}{a^A} \right) \mathbf{e}_i^\gamma \otimes \mathbf{e}_i^\gamma \quad (12)$$

where a^M and c^M are the BCT lattice parameter of the martensite phase, and a^A is the FCC lattice parameter of the austenite phase. The vector \mathbf{e}_i^γ refers to the austenite lattice axis that the Bain contraction from a^A and c^M (while the other two axes elongate from a^A to $\sqrt{2}a^M$) occurred on. The lattice parameters, c^M , a^M and a^A are dependent on carbon content, according to the empirical equations [19]:

$$\begin{aligned} c^M &= 2.861 + 0.116(p_c) = 2.99092\text{\AA} \\ a^M &= 2.861 - 0.013(p_c) = 2.84644\text{\AA} \\ a^A &= 3.548 + 0.044(p_c) = 3.59728\text{\AA} \end{aligned} \quad (13)$$

where $p_c = 1.12\text{wt}\%$ is the carbon concentration in RA for QP980 [18]. Although the carbon concentration should be different for bulk RA and film RA, it does not cause significant differences in the lattice parameters, and only the set of lattice parameters in equation (13) is used in this work.

Several experimental investigations of QP980 using transmission electron microscopy (TEM) [12,22] have revealed the RA transforms into twinned martensite thin-plates, as illustrated in Figure 6. The constitutive modeling of laminated twinned sub-structure transformation has been proposed in the content of crystal plasticity [20,23] and adopted in recent works [17,18]. In this model, we adopt the twinned sub-structure transformation theory and introduce two martensite variants in the transformation-induced \mathbf{F}^{tr} formulation. The equation (10) is modified correspondingly into:

$$[[\mathbf{F}^{tr}]] = \mathbf{R}^{tr} (\lambda_1 \bar{\mathbf{R}} \mathbf{U}^{tr,\gamma_1} + \lambda_2 \mathbf{U}^{tr,\gamma_2}) - \mathbf{I} \quad (14)$$

where γ_1 and γ_2 denote the two martensite variants in twin orientation relation, $\bar{\mathbf{R}}$ represents the relative orientation relation between the two martensite variants, i.e., $\mathbf{e}_i^{\gamma_1} = \bar{\mathbf{R}} \mathbf{e}_i^{\gamma_2}$. \mathbf{U}^{tr,γ_1} and \mathbf{U}^{tr,γ_2} are the Bain deformation tensor for transformation into the two variants (which have different contraction axis, see appendix). λ_1 and λ_2 are the volume fractions of the two twin-variants, subjected to constraint $\lambda_1 + \lambda_2 = 1$. Hanes and Shield's analytical model [16] revealed that for each of the 24 transformation orientation variants, there exists precisely one unique variant to form a twin-pair. The volume fraction of two variants in each twin-pair is also deterministic, resulting in a total of 24 unique twin-sub-structured transformation systems.

$[100]_{\alpha'}$, $[010]_{\alpha'}$ and $[001]_{\alpha'}$. The single grain basis is related to sample basis through the grain orientation matrix (grain Euler angles), i.e., $\mathbf{e}_i = \mathbf{R}^s \mathbf{e}_i^s$. The martensite material reference basis is related to the RA material reference basis through the equation $\bar{\mathbf{R}}$ (see equation (13)).

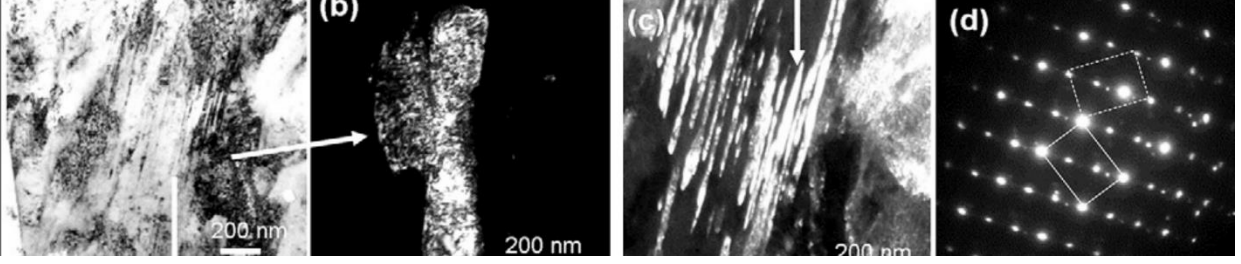


Fig. 6. The TEM observation of deformation-induced martensitic transformation in QP980 showing a twin sub-structure. (a) TEM image of partially-transformed RA during tensile loading (b) untransformed region, and (c,d) twin martensitic structure in the transformed region. The figure is from Xiong et al [12].

It is advantageous to further derive $[[\mathbf{F}^{tr}]]$ in a Schmid tensor-like format for implementation in CPFEM code. This provides an alternative form to equation (14), as follows:[18]:

$$[[\mathbf{F}^{tr}]] = \mathbf{R}^{tr}(\lambda_1 \bar{\mathbf{R}} \mathbf{U}^{tr,\gamma_1} + \lambda_2 \mathbf{U}^{tr,\gamma_2}) - \mathbf{I} = \zeta_{tr} \mathbf{b}^\beta \otimes \mathbf{d}^\beta \quad (15)$$

where β is the selected one of the 24 candidate transformation systems, $\zeta_{tr} = 0.1886$ is the magnitude of deformation during transformation for QP980, \mathbf{b}^β and \mathbf{d}^β are the transformation habit plane normal and the direction vector for transformation-induced deformation, both defined in the single grain basis. Note that \mathbf{b}^β and \mathbf{d}^β are not orthogonal as the transformation-induced deformation involves volumetric change. The 24 orientations of the twinned-transformed martensite systems, and their transformation deformation vectors \mathbf{b}^β and \mathbf{d}^β , as well as the rotation tensors \mathbf{R}^{tr} and $\bar{\mathbf{R}}$ for QP980 are provided in [18] and also tabulated in the appendix for the completeness of the paper.

When numerically implementing the transformation-induced deformation, it isn't feasible to apply $[[\mathbf{F}^{tr}]]$ entirely in a single time increment due to two primary reasons. First, on a physical level, even with our fine model mesh, each element possesses a finite volume or area, making it impossible for the entire element to transform simultaneously. Second, on a numerical level, it would cause convergence issues when refining time steps. As such, we assume that an element, which satisfies the transformation initiation criterion (equation (7)), will complete the transformation over a designated strain increment. Thus, the increment of transformation-induced deformation in each time step after the initiation of transformation is given by:

$$\Delta[[\mathbf{F}^{tr}]] = \frac{\Delta\varepsilon}{\Delta\varepsilon_{MT}} \zeta_{tr} \mathbf{b}^\beta \otimes \mathbf{d}^\beta \quad (16)$$

where $\Delta\varepsilon$ is the increment of applied strain, $\Delta\varepsilon_{MT}$ is a calibratable material parameter, physically representing the total strain increment necessary to achieve full transformation. The effect of modifying $\Delta\varepsilon_{MT}$ is explored in Section 4.1, which shows $\Delta\varepsilon_{MT}$ influence the local stress relaxation in elements

undergoing transformation, thereby playing a crucial role in linking transformation rate to stress-strain behavior.

4.2.2.3 variant selection criterion

The variant selection is governed by maximizing the work which the applied stress has done to assist the transformation and is expressed as:

$$W_i = \mathbf{S} : \mathbf{E}_i^{tr} \quad \text{where} \quad \mathbf{E}_i^{tr} = \frac{1}{2} (\llbracket \mathbf{F}^{tr} \rrbracket^T + \llbracket \mathbf{F}^{tr} \rrbracket + \llbracket \mathbf{F}^{tr} \rrbracket^T \llbracket \mathbf{F}^{tr} \rrbracket) \quad (17)$$

where i is one of the 24 martensite variants and \mathbf{E}_i^{tr} is the Green-Lagrangian type transformation-induced inelastic strain.

4.2.2.4 transition from FCC to BCT crystal structure

The flow rule equation for an austenite element undergoes martensitic transformation can be expressed as:

$$\dot{\mathbf{F}}^{slip} \mathbf{F}^{slip^{-1}} = \begin{cases} \sum_i^{N_{FCC}^{slip}} \dot{\gamma}_\gamma^i \mathbf{m}_\gamma^i \otimes \mathbf{n}_\gamma^i & \text{before MT} \\ f^\gamma \sum_i^{N_{FCC}^{slip}} \dot{\gamma}_\gamma^i \mathbf{m}_\gamma^i \otimes \mathbf{n}_\gamma^i + f^{\alpha'} \left(\sum_i^{N_{BCT}^{slip}} \lambda_1 \dot{\gamma}_{\alpha'_{N1}}^i \hat{\mathbf{m}}_{\alpha'_{N1}}^i \otimes \hat{\mathbf{n}}_{\alpha'_{N1}}^i + \sum_j^{N_{BCT}^{slip}} \lambda_2 \dot{\gamma}_{\alpha'_{N2}}^j \hat{\mathbf{m}}_{\alpha'_{N2}}^j \otimes \hat{\mathbf{n}}_{\alpha'_{N2}}^j \right) & \text{during MT} \\ \sum_i^{N_{BCT}^{slip}} \lambda_1 \dot{\gamma}_{\alpha'_{N1}}^i \hat{\mathbf{m}}_{\alpha'_{N1}}^i \otimes \hat{\mathbf{n}}_{\alpha'_{N1}}^i + \sum_j^{N_{BCT}^{slip}} \lambda_2 \dot{\gamma}_{\alpha'_{N2}}^j \hat{\mathbf{m}}_{\alpha'_{N2}}^j \otimes \hat{\mathbf{n}}_{\alpha'_{N2}}^j & \text{after MT} \end{cases} \quad (18)$$

here, the slip occurs on the 12 $\{111\} \langle 110 \rangle$ FCC slip systems in austenite before the martensitic transformation and occurred in the reorientated BCT martensitic slip systems after transformation. Note that there are two sets of twin-symmetry BCT slip systems after transformation due to the laminated twin martensitic sub-structure. During the martensitic transformation, the element region is partially FCC and partially BCT, thus a volume-fraction-based rule of mixture is used for calculating the plastic flow. The volume fraction of FCC and BCT phases are obtained as:

$$f^{\alpha'} = \frac{\sum \Delta \varepsilon}{\Delta \varepsilon_{MT}}, \quad f^\gamma = 1 - f^{\alpha'}, \quad 0 \leq f^{\alpha'} \leq 1, \quad 0 \leq f^\gamma \leq 1 \quad (19)$$

where $\sum \Delta \varepsilon$ is the total applied strain since triggering the martensitic transformation. The variables $\dot{\gamma}_\gamma^i$, \mathbf{m}_γ^i and \mathbf{n}_γ^i in equation (18) are the slip rate, slip direction vector, and slip plane normal vector of the 12 FCC austenite slip systems. The variables $\{\dot{\gamma}_{\alpha'_{N1}}^i, \hat{\mathbf{m}}_{\alpha'_{N1}}^i, \hat{\mathbf{n}}_{\alpha'_{N1}}^i\}$ and $\{\dot{\gamma}_{\alpha'_{N2}}^j, \hat{\mathbf{m}}_{\alpha'_{N2}}^j, \hat{\mathbf{n}}_{\alpha'_{N2}}^j\}$ are the slip rate, slip direction vector, and slip plane normal vector of the 24 BCT martensite slip systems in the two twin variants, leading to a total of 48 slip systems. The orientation of the new BCT slip system is defined by:

$$\begin{aligned}\hat{\mathbf{m}}_{\alpha'}^{i=1\dots24} &= \mathbf{Q}_1^{tr} \mathbf{m}_{\alpha',0}^{i=1\dots24} & \hat{\mathbf{n}}_{\alpha'}^{i=1\dots24} &= \mathbf{n}_{\alpha',0}^{i=1\dots24} \mathbf{Q}_1^{tr^{-1}} \\ \hat{\mathbf{m}}_{\alpha'}^{i=25\dots48} &= \mathbf{Q}_2^{tr} \mathbf{m}_{\alpha',0}^{i=1\dots24} & \hat{\mathbf{n}}_{\alpha'}^{i=25\dots48} &= \mathbf{n}_{\alpha',0}^{i=1\dots24} \mathbf{Q}_2^{tr^{-1}}\end{aligned}\quad (20)$$

where $\mathbf{m}_{\alpha',0}^i$ and $\mathbf{n}_{\alpha',0}^i$ are reference slip direction vector and slip plane normal vector of the 24 BCT martensite slip systems in the single grain basis; \mathbf{Q}_1^{tr} and \mathbf{Q}_2^{tr} are the rotation tensor between the austenite material reference basis and the transformed martensite material reference basis. Their values depends on the specific martensite variant chosen for transformation, and is expressed as:

$$\mathbf{Q}_1^{tr} = \mathbf{R}^{tr} \bar{\mathbf{R}} \mathbf{R}^*; \quad \mathbf{Q}_2^{tr} = \mathbf{R}^{tr} \mathbf{R}^* \quad (21)$$

where \mathbf{R}^{tr} (the rotation tensor to account for the orientation relationship between the austenite matrix and the martensite twin variant 1) and $\bar{\mathbf{R}}$ (rotation tensor between twin variant 1 and variant 2) have been previously introduced. \mathbf{R}^* is the rotation tensor due to the Bain deformation[18], which depends on the specific axes of austenite FCC lattice that undergoes Bain contraction (consistent with equation (12)), and is expressed as:

$$\mathbf{R}_{(1)}^* = \begin{bmatrix} 1 & 0 & 0 \\ 0 & \frac{\sqrt{2}}{2} & -\frac{\sqrt{2}}{2} \\ 0 & \frac{\sqrt{2}}{2} & \frac{\sqrt{2}}{2} \end{bmatrix}, \quad \mathbf{R}_{(2)}^* = \begin{bmatrix} \frac{\sqrt{2}}{2} & 0 & \frac{\sqrt{2}}{2} \\ 0 & 1 & 0 \\ -\frac{\sqrt{2}}{2} & 0 & \frac{\sqrt{2}}{2} \end{bmatrix}, \quad \mathbf{R}_{(3)}^* = \begin{bmatrix} \frac{\sqrt{2}}{2} & -\frac{\sqrt{2}}{2} & 0 \\ \frac{\sqrt{2}}{2} & \frac{\sqrt{2}}{2} & 0 \\ 0 & 0 & 1 \end{bmatrix} \quad (22)$$

Here, the subscript refers to the FCC lattice axis of Bain contraction. The lattice rotation also affects the elastic stiffness tensor, which is expressed as:

$$\hat{\mathbb{C}}_{\alpha'_N}^e = \lambda_1 \mathbf{Q}_1^{tr} \mathbf{Q}_1^{tr} \mathbb{C}_{\alpha'_N}^e \mathbf{Q}_1^{trT} \mathbf{Q}_1^{trT} + \lambda_2 \mathbf{Q}_2^{tr} \mathbf{Q}_2^{tr} \mathbb{C}_{\alpha'_N}^e \mathbf{Q}_2^{trT} \mathbf{Q}_2^{trT} \quad (23)$$

where $\hat{\mathbb{C}}_{\alpha'_N}^e$ is the effect fourth-order elastic stiffness tensor of the twin-sub-structure martensite lattice, and $\mathbb{C}_{\alpha'_N}^e$ is the reference fresh martensite elastic stiffness matrix in martensite material reference basis.

Finally, the power-law equation (4) and generalized Voce hardening equation (5) are used to model the slip rate and hardening behavior in addition to the transformation, with different sets of yield and hardening parameters for the austenite lattice and after it transformed to the fresh martensite lattice. Considering the fresh martensite after the mechanical-induced transformation often encompasses a high dislocation density, the primary hardening variable-the accumulated plastic strain-inherits hardening from the austenite lattice, as expressed by the following:

$$\hat{\gamma} = \sum_i^{Nslip_{FCC}} \int_0^{t_{MT,0}} |\dot{\gamma}^i| dt + \sum_i^{Nslip_{BCT}} \int_{t_{MT,0}}^t (\lambda_1 \dot{\gamma}_{\alpha_{N1}}^i + \lambda_2 \dot{\gamma}_{\alpha_{N2}}^i) dt \quad (23)$$

where $t_{MT,0}$ is the moment of martensitic transformation initiation. The first term of the right-hand-side of equation (23) corresponds to the accumulated slip inherited from the plastic deformation in austenite, and the second term corresponds to accumulated slip in fresh martensite.

4.2.3 Crystal plasticity model for combined tempered martensite and film austenite phases

Owing to the exceedingly fine thickness of the film RA, it is impractical to explicitly model the morphology of the tempered martensite-film austenite laths. Instead, an iso-strain (affine transformation) assumption is employed to model the homogenized tempered martensite and film austenite laths. Mustafa et al [60] demonstrated that for a finely laminated two-phase structure, the iso-strain assumption yields less than a 10% error compared to the more sophisticated, yet computationally complex homogenization approaches such as the asymptotic expansion-based homogenization method. Consequently, the iso-strain method is chosen for this work. The deformation gradient of tempered martensite $\mathbf{F}^{\alpha'_T}$ and film austenite phases \mathbf{F}^{γ_F} therefore follow:

$$\mathbf{F}^{\alpha'_T} = \mathbf{F}^{\gamma_F} = \mathbf{F} \quad (24)$$

Here, \mathbf{F} is the deformation gradient of an integration point. The stress at the integration point is computed as:

$$\boldsymbol{\sigma}^{ave} = f^{\gamma_F} \boldsymbol{\sigma}^{\gamma_F} + f^{\alpha'_T} \boldsymbol{\sigma}^{\alpha'_T} \quad (25)$$

where $\boldsymbol{\sigma}^{\gamma_F}$ and $\boldsymbol{\sigma}^{\alpha'_T}$ are Cauchy stress of tempered martensite and film austenite, respectively; f^{γ_F} and $f^{\alpha'_T}$ are the corresponding volume fraction of the two phases, adhering to the condition that $f^{\gamma_F} + f^{\alpha'_T} = 1$. Similar to pre-existing fresh martensite phase, the Cauchy stress of the tempered martensite phase is computed using equation (1-6). The film-austenite phase is assumed to obey the same transformation laws and constitutive laws as the bulk austenite phase, but with a different transformation initiation energy criterion ΔG_{crit}^{eff} due to the difference in chemical composition (7).

4.2.4 Finite element pseudo-3D model and boundary conditions

A $50\mu\text{m} \times 50\mu\text{m}$ EBSD image of QP980 is converted to a two-dimensional FE model. In literature [24–27], three-dimensional synthetic microstructures are frequently employed to simulate the polycrystalline materials. However, creating a complex, multi-phase synthetic microstructure akin to QP980 poses a significant challenge, especially when trying to ensure that the synthetic microstructure accurately represents the spatial distribution and correlation of each phase. For instance, the stability of γ_B phase fluctuates depending on its location within the ferrite or martensite matrix, a crucial consideration for this study. Therefore, we have chosen to model the exact microstructure as derived from EBSD under a generalized plane strain condition. The generalized plane strain condition, an extension of the plane strain,

allows for a uniform but not necessarily zero strain in the thickness direction. This condition offers an intermediate level of constraint, falling between plane stress and plane strain conditions. The FE mesh consists of 250×250 four-node-quadrilateral elements, and each element has a initial length of 200nm, as shown in Figure 7. The crystallographic orientation of each element was assigned directly from the EBSD image, and the film austenite portion in the combined $\alpha'_T + \gamma_f$ element is from the reconstructed parent austenite grain map (see Figure 5). Under the isothermal room temperature condition, the model were subjected to tensile and compressive loads with a constant strain rate $\dot{\epsilon} = 1 \times 10^{-3}$, applied by specifying displacement on edge nodes in X-direction (RD). The Y-direction (TD) edges were set to traction-free, as shown in Figure 7.

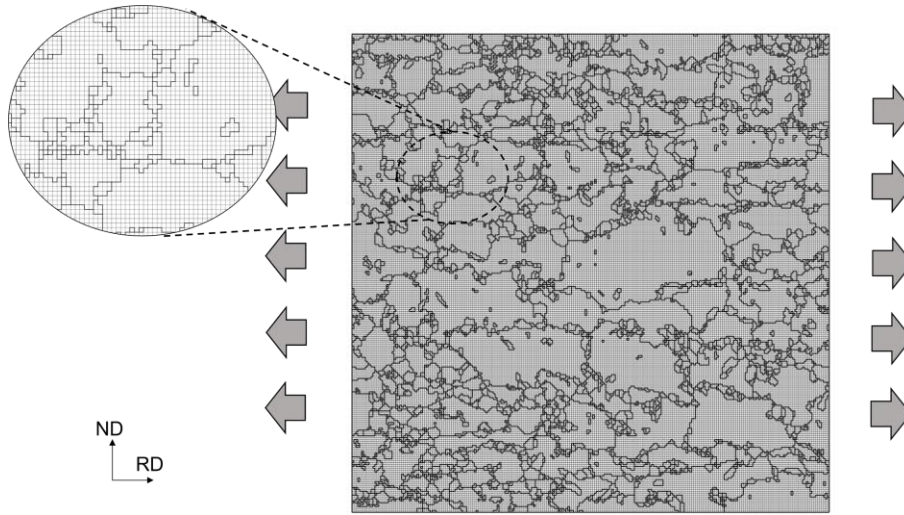


Fig. 7. FE mesh for QP980 model in CPFEM simulation.

4.3 Constitutive parameters determination by integrated in-situ neutron diffraction and crystal plasticity modeling.

The model is calibrated and validated against the experimental stress-strain data sourced from uniaxial tension and compression tests, along with the measurements of in-situ HEXRD from a synchrotron source. In this section, we first present a sensitivity study of the calibratable model parameters, shedding light on the impact of each parameter on transformation kinetics and stress-strain behavior. Then, we compare the calibrated model to experimental results by scrutinizing the stress-strain curves, lattice strain on different lattice planes for each individual phase, and the evolution of retained austenite evolution fraction. Lastly, we delve into a discussion on a few key mechanisms affecting the martensitic transformation, as indicated by the model results.

4.3.1 Model parameters sensitive study

The calibratable parameters within the model can be summarized as follows:

- Effective critical transformation energy for bulk and film austenite $\{ \Delta G_{crit,B}^{eff}, \Delta G_{crit,F}^{eff} \}$
- The fitting parameters for mechanical energy in transformation criterion $\{ c_1, c_2, c_3, c_4 \}$
- Transformation rate-related parameter $\Delta \varepsilon_{MT}$
- Slip system yield stress and hardening parameters $\{ g_0^i, g_s^i, \theta_0^i, \theta_1^i \}$ for ferrite, austenite, tempered martensite and fresh martensite phases.

To understand the effect of each parameter on the local and holistic behavior of QP980, especially with respect to the transformation kinetics and stress-strain response, each parameter is perturbed individually and the change to the simulation results is examined. The “reference” model parameter values are enumerated in Table 2. It should be noted that, with the target of best illustrating the impact of each parameter, these “reference” values should ideally be as precise as possible. Therefore, the final calibrated results are employed as the "reference" in this context, despite it being contrary to the chronological sequence of the actual work. Hence, the sensitivity study figures depicted here are retrospective.

We start by presenting the local stress-strain curve in an austenite element during the martensitic transformation process, as shown in Figure 8. With the inelastic Bain deformation induced by transformation, the austenite element experiences a local stress relaxation during the transformation, as marked in Figure 8a. Subsequently, the element transits to a fresh martensite phase and experience a much higher hardening stress. The parameter $\Delta \varepsilon_{MT}$ dominates the magnitude of stress relaxation, as shown in Figure 8b.

The initiation of the martensitic transformation is governed by a combination of two primary factors: (a) the amount of load conveyed to the austenite element from its surrounding matrix, and (b) the parameters associated with transformation stability, which includes $\{ \Delta G_{crit,B}^{eff}, \Delta G_{crit,F}^{eff}, c_1, c_2, c_3, c_4 \}$. Figure 9a displays the evolution of RA volume fraction under uniaxial tensile load with different values of $\{ \Delta G_{crit,B}^{eff}, \Delta G_{crit,F}^{eff} \}$. The lower values of $\{ \Delta G_{crit,B}^{eff}, \Delta G_{crit,F}^{eff} \}$ result in an accelerated transformation rate. The rapid martensitic transformation, which leads to stress relaxation across multiple austenite elements, results in a decreased hardening rate in global stress throughout the transformation period, as shown in Figure 9b. Another notable effect of lower $\{ \Delta G_{crit,B}^{eff}, \Delta G_{crit,F}^{eff} \}$ values is that the accelerated transformation rate induces a higher proportion of fresh martensite within the microstructure, which, in turn, leads to an increased hardening stress in the subsequent stage of stress-strain curves, a phenomenon also observed in Figure 9b. Additionally, the bulk RA and film RA can have different stability by setting the

$\Delta G_{crit,F}^{eff} : \Delta G_{crit,B}^{eff}$ ratio, which influences the fraction of remaining austenite and changes the slope of the total austenite volume fraction evolution curve, as demonstrated in Figures 9c and 9d.

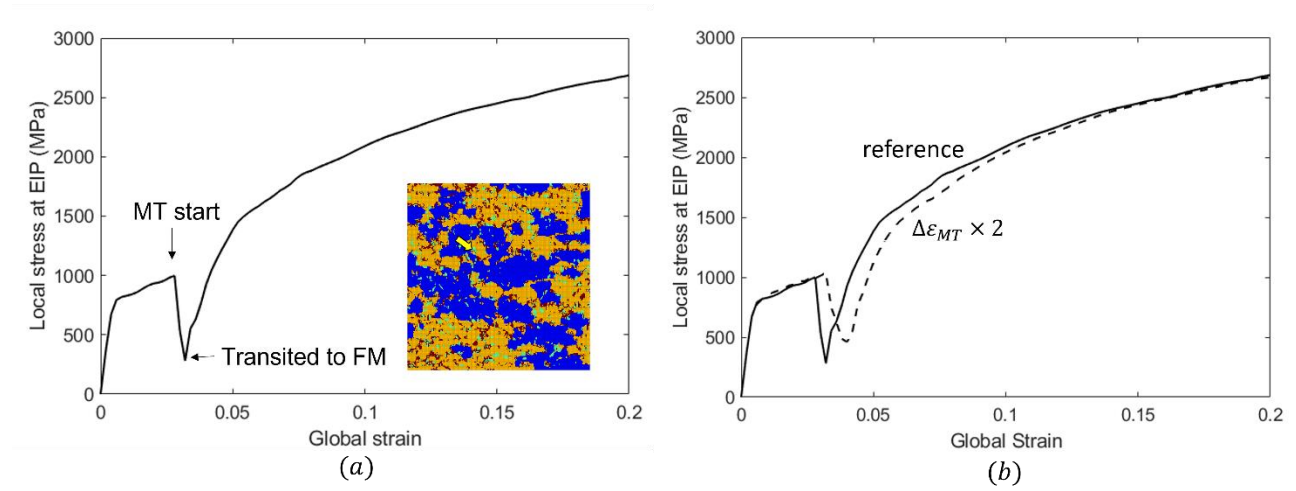


Fig. 8. (a) Local stress evolution in a bulk RA element (marked in microstructure); (b) influence of calibratable parameter $\Delta\epsilon_{MT}$ to transformation-induced local stress relaxation.

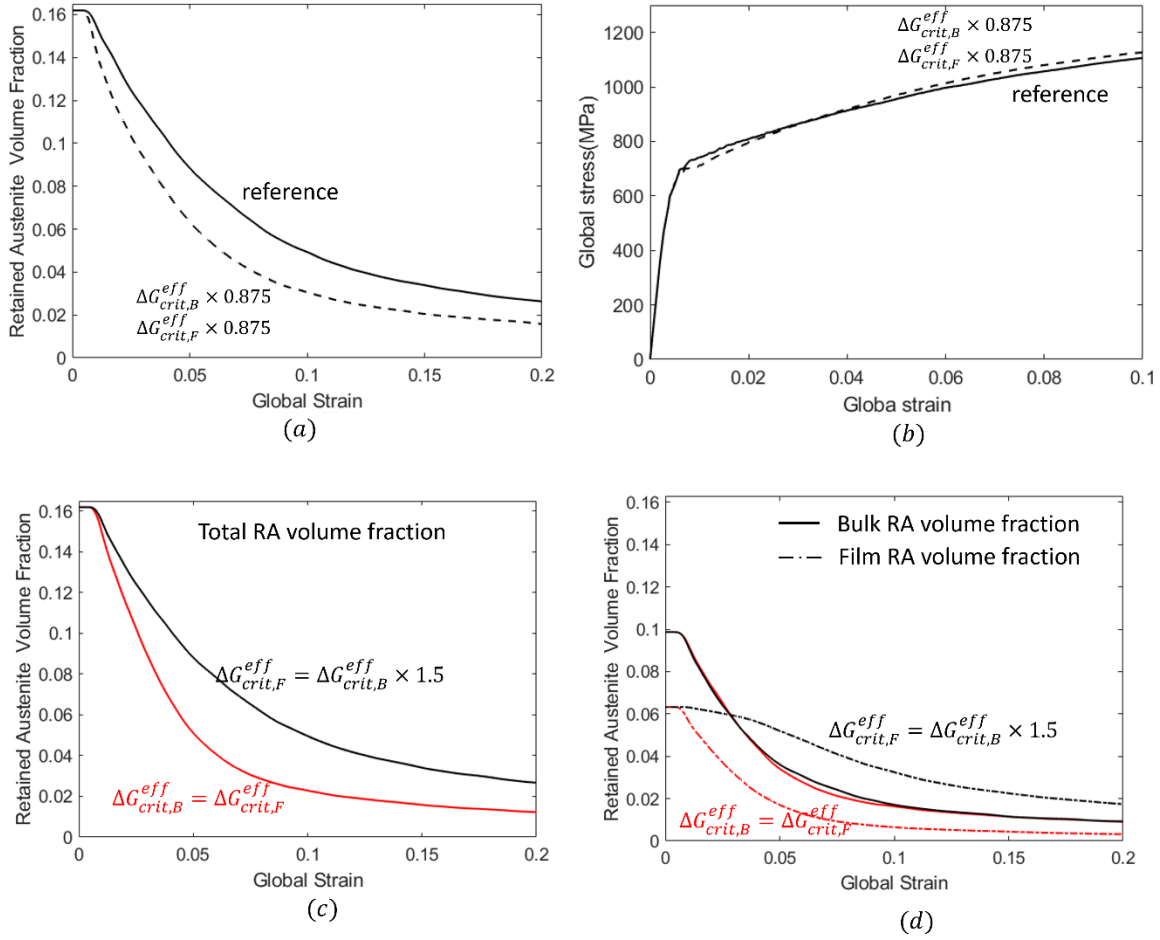


Fig. 9. Sensitivity of parameters $\{\Delta G_{crit,B}^{eff}, \Delta G_{crit,F}^{eff}\}$ on (a,c,d) RA volume fraction evolution and (b) tensile stress-strain curve. The reference value is $\Delta G_{crit,B}^{eff} = 800\text{J/mol}$, $\Delta G_{crit,F}^{eff} = \Delta G_{crit,B}^{eff} \times 1.5$.

The parameters $\{c_1, c_2, c_3, c_4\}$ determines the influence of the stress state on transformation kinetics. Specifically, c_1 governs the effect of von Mises stress on the transformation process, while c_2 determines the impact of hydrostatic stress on the transformation. It is important to note that the latter results in a tension-compression asymmetric behavior of the material. The stress-strain curves under uniaxial tensile and compressive load, as shown in Figures 10a and 10b, demonstrate that by increasing $c_1 : c_2$ ratio the tension-compression asymmetry is reduced. The parameters $\{c_3, c_4\}$ correspond to the higher-order effect of von Mises stress on transformation, however, the calibration of $\{c_3, c_4\}$ requires more extensive experiment data and are not considered in this work. Instead the reference values of $\{c_3, c_4\}$ in Behera et al [7] are adopted.

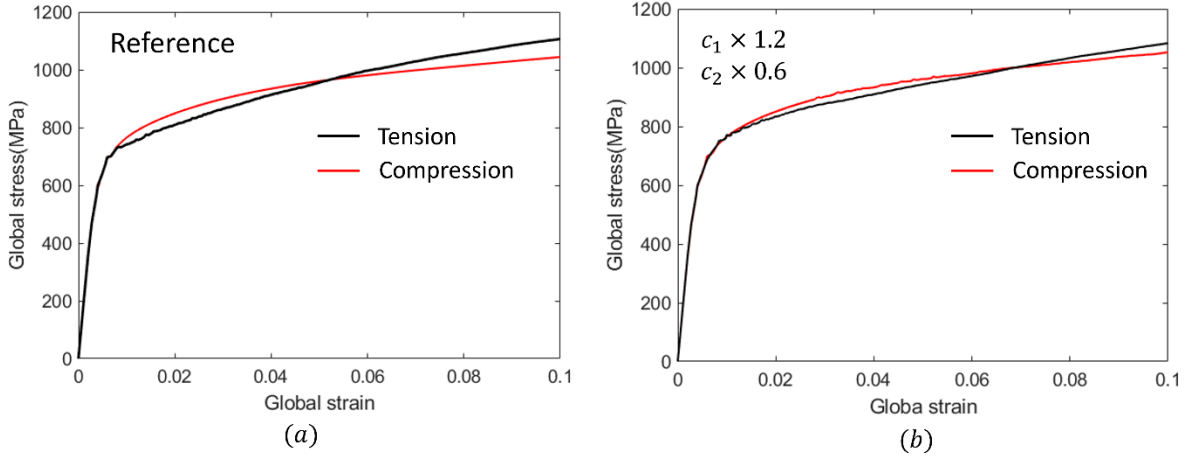


Fig. 10. Sensitivity of tension-compression asymmetric stress-strain curves to $c_1:c_2$ ratio.

Finally, the parameters $\{g_0^i, g_s^i, \theta_0^i, \theta_1^i\}$ for slip system yield and hardening stress in each phase are calibrated by matching the lattice strain to the measurement from in-situ HEXRD, following the approach as described in literature [27–29].

Table 2: Calibrated model parameters

| <i>Martensitic transformation</i> | $\Delta G_{crit,B}^{eff}$ | $\Delta G_{crit,F}^{eff}$ | c_1 | c_2 | c_3 | c_4 | $\Delta \varepsilon_{MT}$ |
|--|---------------------------|---------------------------|--------------|--------------|--------|----------|---------------------------|
| <i>model parameters:</i> | 800J/mol | 1200J/mol | 0.467 | 28.77 | -185.3 | -0.00152 | 0.5% |
| <i>Ferrite yield and hardening</i> | g_0^i | g_s^i | θ_0^i | θ_1^i | | | |
| <i>parameters:</i> | 168MPa | 70MPa | 1200MPa | 10MPa | | | |
| <i>Tempered martensite yield and hardening parameters:</i> | g_0^i | g_s^i | θ_0^i | θ_1^i | | | |
| | 326MPa | 80MPa | 1000MPa | 10MPa | | | |
| <i>Fresh martensite yield and hardening parameters:</i> | g_0^i | g_s^i | θ_0^i | θ_1^i | | | |
| | 400MPa | 500MPa | 3500MPa | 500MPa | | | |
| <i>Austenite yield and hardening parameters:</i> | g_0^i | g_s^i | θ_0^i | θ_1^i | | | |
| | 241MPa | 80MPa | 1600MPa | 450MPa | | | |

4.3.2 Comparison between experiment and model results

The experiment data available for model calibration consists of stress-strain curves obtained from uniaxial tension and compression tests, as well as the lattice strain data and the RA volume fraction evolution data obtained from in situ HEXRD measurement during uniaxial tension test.

It is worthy to briefly compare the method of calculating lattice strain and RA volume fraction from HEXRD versus CPFЕ models. The HEXRD enables a volumetric diffraction measurement via penetration of the test sample [28]. The diffraction pattern is obtained from the integration of the Debye rings associated with different phase and their different orientated lattice planes. During the loading of the test sample, the shifting of the diffraction pattern due to elastic straining of the lattice (change of spacing) are continuously recorded, and the lattice strain $\varepsilon_{\{hkl\}}$ of a $\{hkl\}$ plane can be calculated from either the change of lattice spacing d_{hkl} or diffraction angle θ_{hkl} . The lattice strain is usually calculated along a fixed direction e.g., loading direction (LD), in which case only an arc of Debye ring confined to $\pm\eta^\circ$ angle along loading direction is integrated for computing the lattice strain. The evolution of the volume fraction of the austenite phase can be obtained from the change of its diffraction peak intensity, which enables the tracking of transformation rate.

In CPFЕ simulation, the computed lattice strains are calculated by averaging the elastic strain of the elements that have their $\{hkl\}$ lattice plane normal aligned within a tolerance of $\pm\eta$ angle along LD. The calculation can be expressed as:

$$\varepsilon_{\{hkl\}} = \sum_{i=1}^{\# \text{ of elements}} \frac{V_i}{V_N} \mathbf{n}^{LD} : \mathbf{E}_i^e : \mathbf{n}^{LD} \quad \forall i \in \mathbb{N}_\eta \quad (27)$$

where \mathbf{E}^e is the elastic Green-Lagrangian strain, $\mathbb{N}_\eta = \{\theta_i^{\{hkl\}/LD} \leq \eta\}$ is the assembly of the elements satisfying the orientation requirement, and $\theta_i^{\{hkl\}/LD}$ is the angle between the $\{hkl\}$ lattice plane normal of element i and LD. V_i is the volume of an element i , V_N is the total volume of all elements in \mathbb{N}_η , and \mathbf{n}^{LD} is the unit vector along the LD. Note that, the tolerance η for HEXRD experiment is set to $\pm 2^\circ$; however, the simulation model size is smaller and doesn't contain a sufficient number of grains satisfying the same criterion, thereby η is increased to $\pm 10^\circ$. The evolution of RA volume fraction is straightforward and by tracking the total number of RA elements, as in the simulation once an RA element is transformed it is counted as fresh martensite elements from the time step of completing transformation.

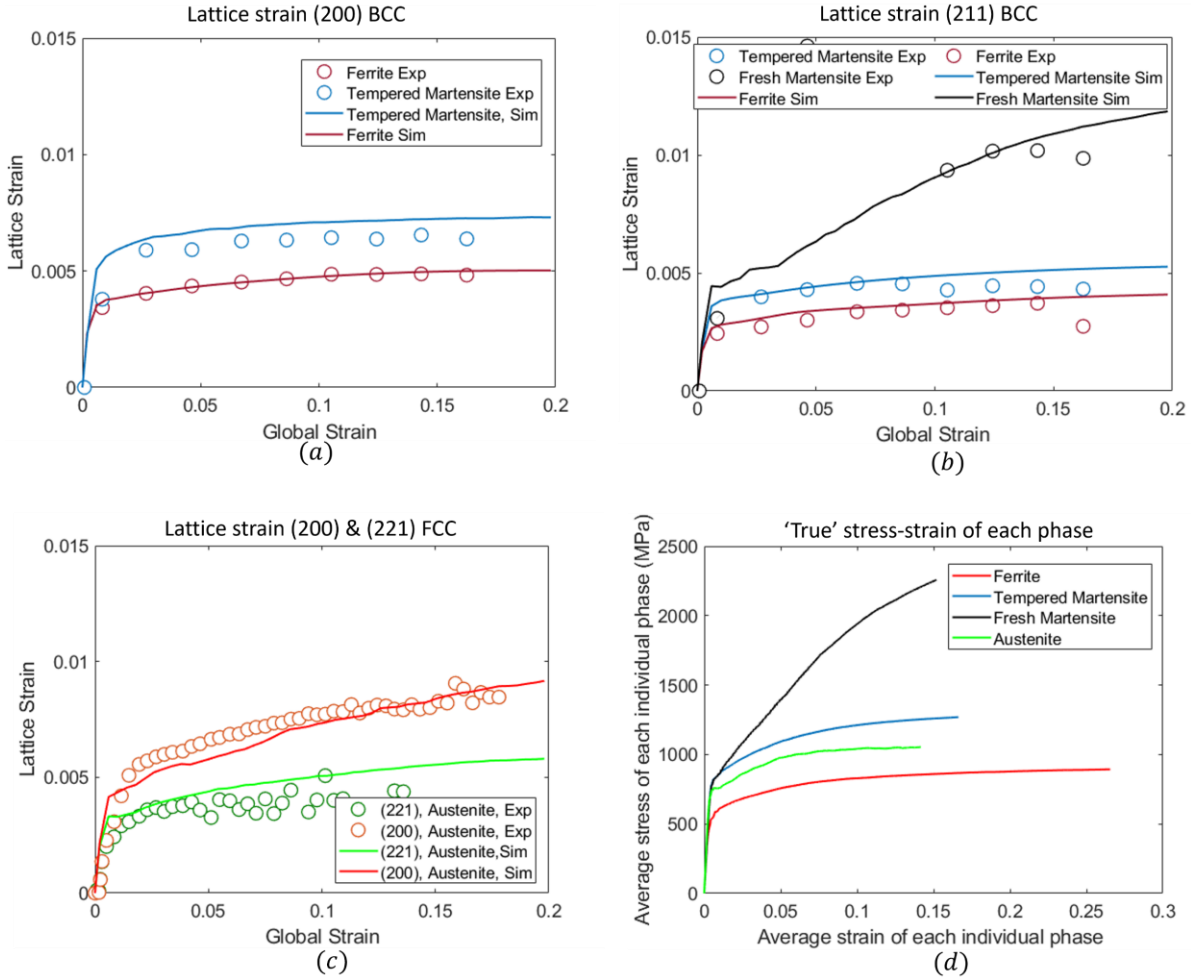


Fig. 11. Lattice strain comparison.

The comparison between the lattice strain measured from HEXRD and the simulated results is presented in Figure 11a and 11b for $\epsilon_{\{200\}}$ and $\epsilon_{\{211\}}$ of BCC and BCT phases, respectively; and the lattice strain for the austenite phase is compared in Figure 11c. It is worth noting that the $\epsilon_{\{200\}}$ lattice strain for the fresh martensite phase is of low quality and thus not included in the figure. Satisfactory matching is obtained for all phases, except the simulated $\epsilon_{\{200\}}$ of tempered martensite, as well as $\epsilon_{\{221\}}$ of austenite phase are slighter higher than HEXRD measurement. The simulated 'true' stress-strain for each individual phase, which is computed by averaging the loading direction stress and strain component using only elements in the corresponding phase, is shown in Figure 11d. The stress and strain partition between different phases is quite obvious in 'true' stress-strain curves of individual phases. The ferrite phase is the softest phase and has the lowest yield and hardening stress; the 'true' strain of the ferrite phase is the highest, which means more deformation participated in the ferrite phase than other phases. The austenite phase (which is volume-averaged using both bulk and film RA elements) has a slightly lower yield and hardening stress than the

tempered martensite phase. The austenite phase also has the lowest ‘true’ strain, but it is because most austenite phases are transformed into fresh martensite before they could undertake a large deformation. The transformed fresh martensite exhibits the highest hardening stress, which is attributed to the significant hardening resulting from the high dislocation density attained after transformation [28].

The global stress-strain curves for uniaxial tension and compression simulations are compared to experimental measurement in Figure 12a, and the corresponding RA volume fraction is shown in Figure 12b. The model effectively captures the stress-strain asymmetry observed in tension and compression tests, which is attributed to the different transformation kinetics under the two strain paths. Under compressive loading, the martensitic transformation is inhibited due to the obstructive role of the compressive stress state to the Bain deformation, and the material exhibits a stress-strain curve that is less influenced by the transformation. On the other hand, during tension, the initial hardening rate is remarkably reduced, attributed to a substantial fraction of austenite undergoing martensite transformation. The stress is locally relaxed near the austenite regions of transformation, while other regions experience strain-hardening. After ~5% strain, many austenites have already transformed into fresh martensites and exhibit a high hardening stress, resulting in a higher global stress that exceeded the compression stress-strain curve.

It should be noted that although there is no direct data available for the austenite volume fraction evolution in the compression loading test, the simulated difference in the tension-compression austenite evolution trend is close to the trend in experiment data in Feng et al [30] despite of different setup. Therefore, the simulated austenite volume fraction evolution for compression is expected to be trustworthy for further analysis. This expectation is also based on the good agreement between the simulated lattice strain, the evolution of austenite volume fraction in tension, and the stress-strain tension-compression asymmetry in stress-strain behavior.

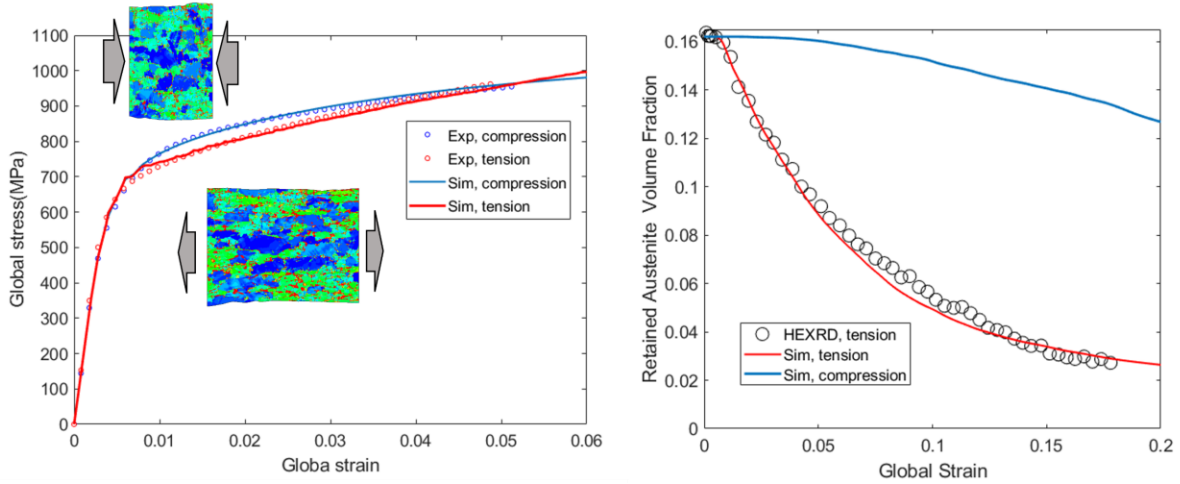


Fig. 12. (a) Stress-strain curves, and (b) the corresponding RA volume fraction evolution.

4.3.3 Local stress and strain state investigation

In addition to the average lattice strain for each phase, the CPFE simulation provides insights into the local stress distribution within the microstructure. Figures 13 and 14 plots the distribution of von Mises stress, hydrostatic stress and effective strain in undeformed configuration (for ease of comparison) at 2% applied strain for tension and compression simulations, respectively. Here the effective strain is defined as $\varepsilon_{eff} = \sqrt{\sum_{i,j} \frac{2}{3} (E_{ij})^2}$. The 2% strain is chosen for visualization because it is the moment the tension-compression asymmetry is obvious. Furthermore, the statistics of these stress and strain invariants at 1%, 2% and 5% strain for each phase are plotted using histograms in Figures 15 and 16. A few observations are made from the results:

1. The stress and strain distribution in QP980 microstructure is quite heterogeneous.
2. The von Mises stress distribution exhibited a very clear stress-partitioning among different phases, while the hydrostatic stress is not so obvious. This is likely because the shear stress-state is dominated by the resistance to slip in each phase, while hydrostatic stress is due to the interaction between neighboring phases.
3. From the histogram, the strain distribution has a clear trend that more deformation is partitioned to ferrite phase with increasing load. Relate that to the strain distribution in Figure 13 and 14, it is noticed the strain like to form concentration ‘bands’ in ferrite regions especially in narrow channels surrounded by martensite.

4. Comparing the strain distribution in compression and tension (Figure 13 vs 14), there are many local spots with high strain concentration in tension case, which correspond to the austenite grains going through the transformation and induced local Bain deformation.
5. Under both tension and compression, the distribution of von Mises stress is similar, except that the von Mises stress is more heterogeneous due to a high fraction of fresh martensite and its high hardening rate.
6. In hydrostatic stress distribution, the austenite phase in tension at 5% strain has a decreased average hydrostatic stress than 2% strain. This is because many austenite regions with high hydrostatic stress has already transformed, leaving most low hydrostatics stress austenite regions remained.
7. In hydrostatic stress distribution for tension case (Figure 13d), while most regions have tensile (positive) hydrostatic stress state, some local regions are in compressive (negative) hydrostatic stress state. Those compressive stress state could raise due to two mechanisms: I) during an uniaxial tensile loading, the irregular shape of soft/hard phases will try to locally rotate in addition to stretching, and the rotation can cause a local compressing onto the neighboring phase. This is a mechanism similar to the soft-hard constitutions interaction in metal-metal composites [31]. II) the austenite transformation induces inelastic Bain deformation and cause local stress-relaxation and in some local regions even local compressive stress-state. These two types of mechanisms can be differentiated in the hydrostatic stress map: the local compressive stress induced by transformation will vanish with increased load, while the type I compressive stress state will remain (and increase) with increased load. Furthermore, under compression, there are also local regions that are in tensile stress-state as shown in Figure 13d, and those regions also correspond to the type I mechanism in an opposite way.

The above model observations highlight the importance of interaction between neighboring phases on the local stress-state. Especially, the interaction of the austenite phase with its surrounding matrix can influent the transformation kinetics, which is critical for strain-path dependence behavior of QP980, and is investigated in next section.

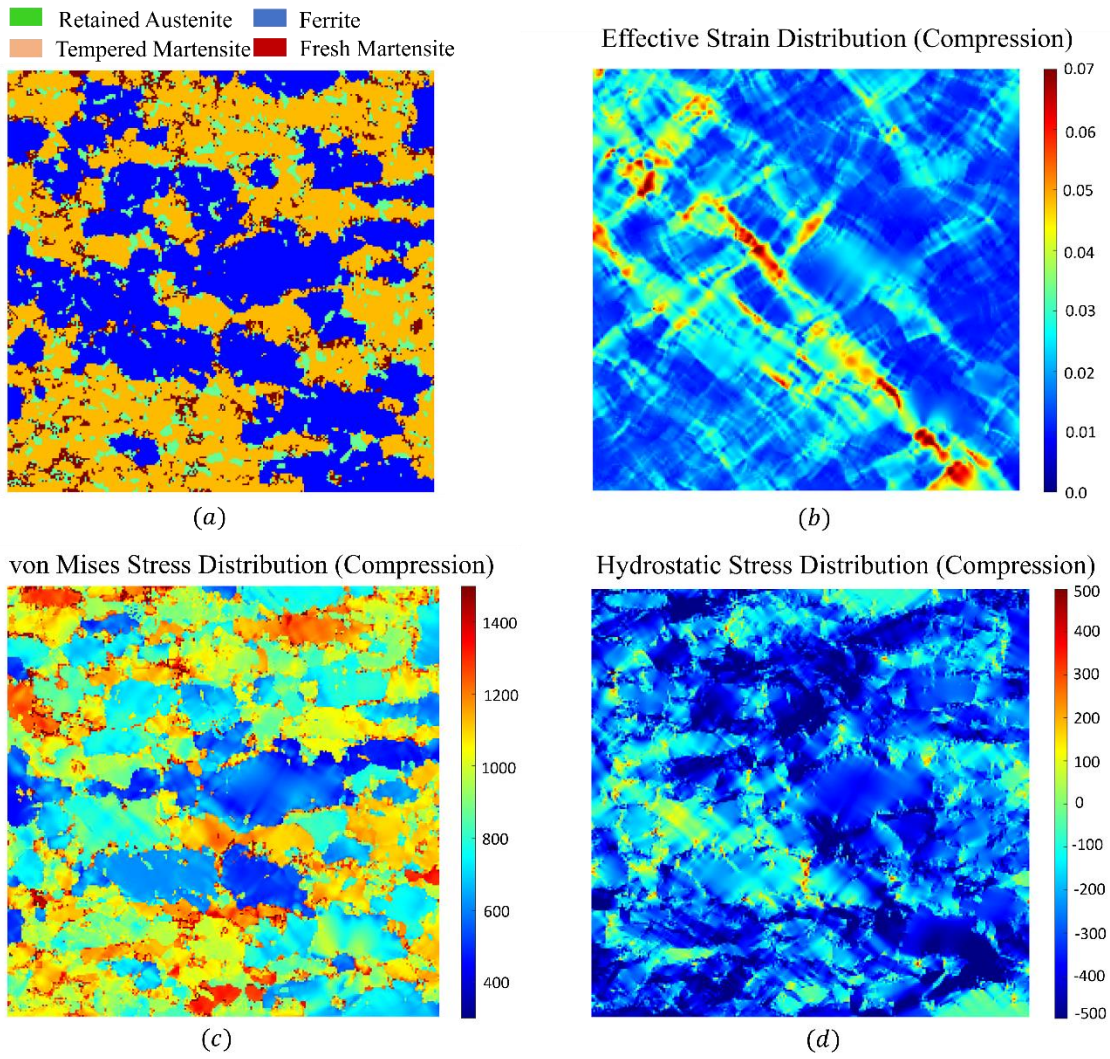


Fig. 13.

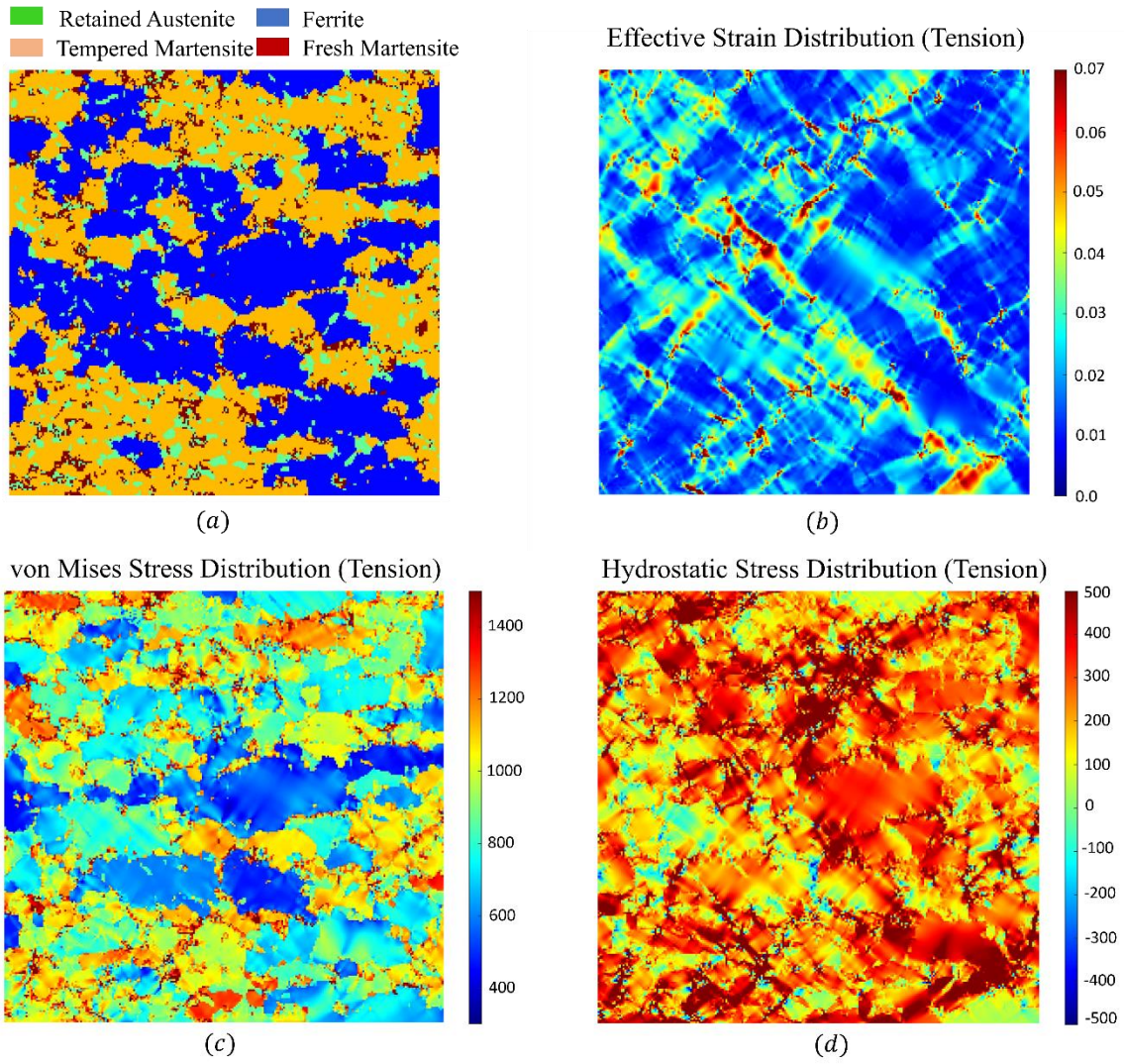


Fig. 14.

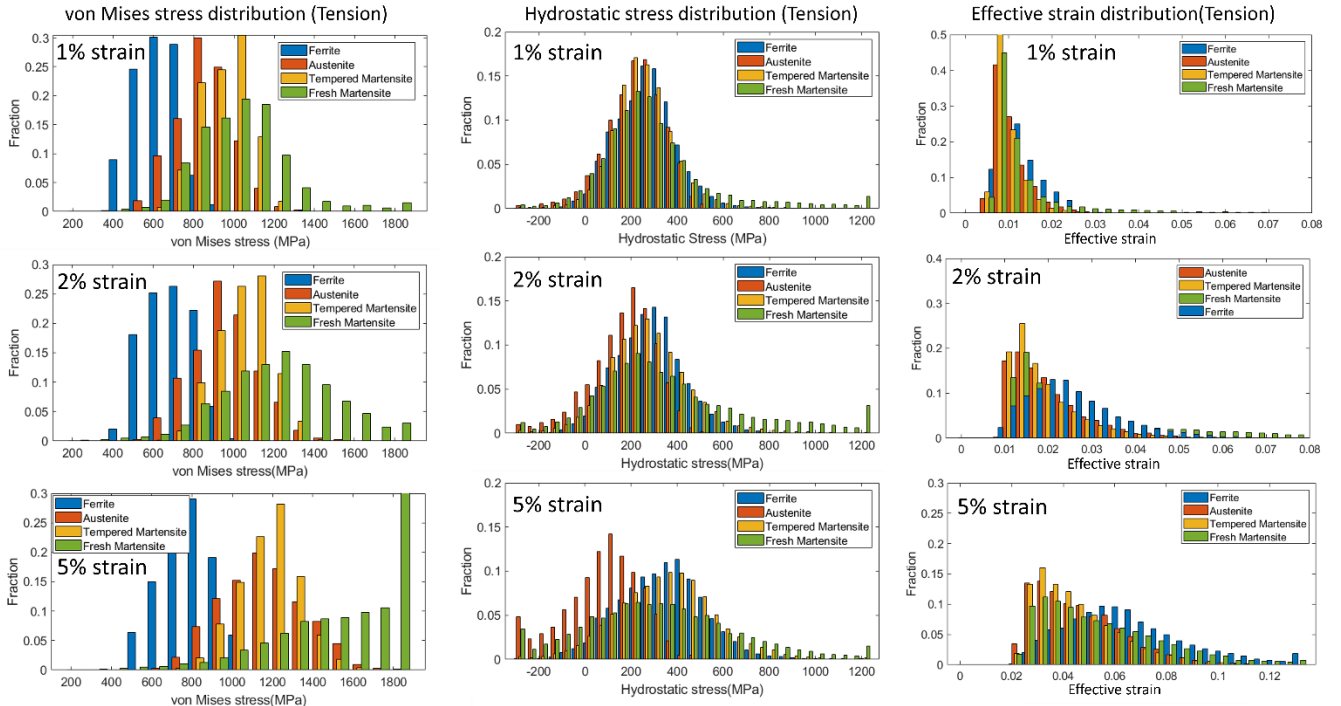


Fig. 15.

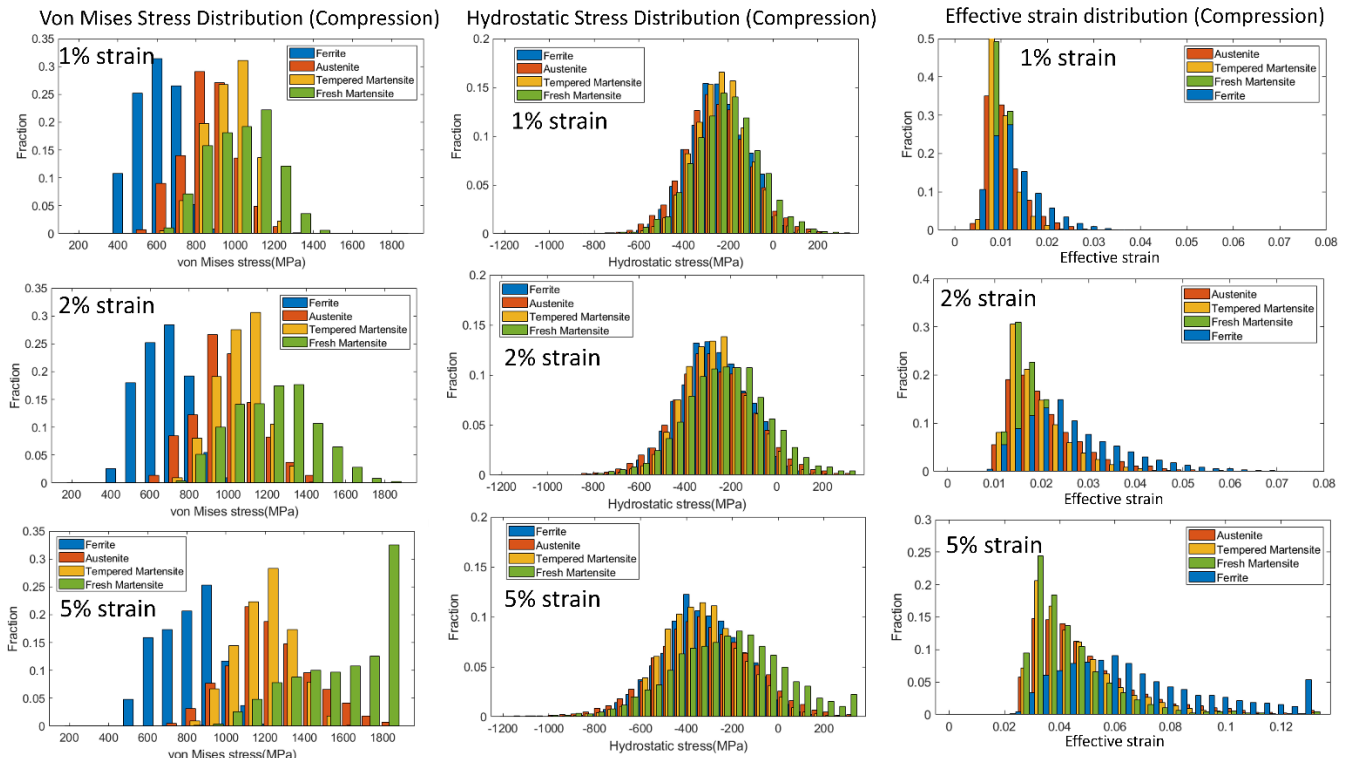


Fig. 16.

4.3.4 Effect of surrounding matrix on stability of RA

We focus on analyzing the bulk RA as their surrounding matrix is explicitly modeled in CPFE framework. The bulk RA, surrounded by ferrite matrix (type I) and martensite (including both tempered and fresh) matrix (type II), are separately identified and highlighted in Figure 17. The rest of the bulk RA are located in a mixed matrix and categorized as type III. Figure 18a and 18b shows the separate volume fraction evolution for the three types of RA under tensile and compressive loading, respectively. In tension, the RA in ferrite matrix has the highest stability, at 20% applied strain there is still a significant amount of untransformed RA in ferrite matrix remained. The RA in martensite matrix has the lowest stability and are mostly transformed at 20% applied strain. This trend is quite consistent with the trend observed in tension-test EBSD-based measurement in Kang et al [32], despite the number has some mismatch which is likely because both the model and EBSD only covers a small area and statistically insufficient. However, under compressive loading, the simulation predicted trend of RA stability is opposite to tension case: the RA in ferrite matrix transformed more than the RA in martensite matrix, despite both didn't transform as much as under tensile loading.

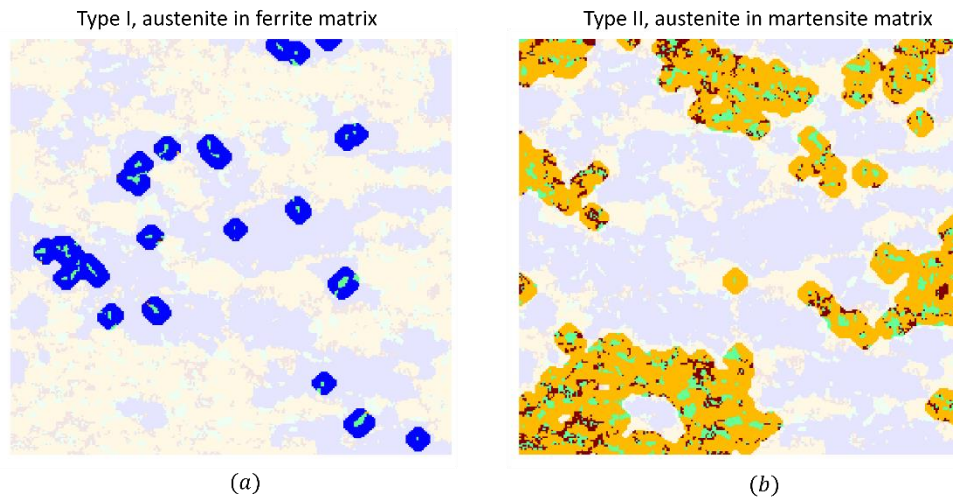


Fig. 17.

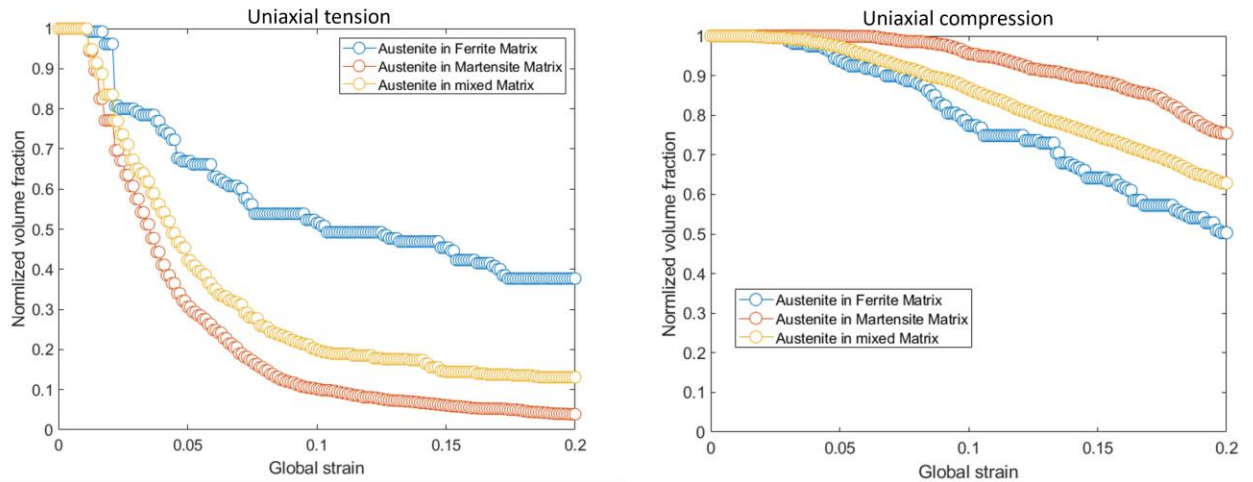


Fig. 18.

The stress state of the bulk RA surrounded by ferrite and martensite matrix are compared in Figure 19 for tensile loading case, and in Figure 20 for compressive loading case. The following observation is made:

1. The von Mises stress distribution for the type I (in ferrite matrix) and type II (in martensite matrix) RA are not very different, which is true for both compression and tension cases.
2. The hydrostatic stress has a clear difference between the type I and type II RA. The type I RA has clearly a lower hydrostatic stress (magnitude, or absolute value) than type II RA under tension and compression. In addition, more type I RA has an opposite hydrostatic stress state (under tensile load, more type I RA are in compressive stress state, and vice versa).
3. In tension, the lower tensile hydrostatic stress inhibited the type I RA from transformation and resulting to a higher stability in Figure 18a. In contrast, under compressive load, the lower compressive hydrostatic stress from ferrite matrix played an opposite effect and resulted in a higher transformation rate, as shown in Figure 18b.
4. As the applied strain increases from 2% to 5% in tensile loading case, the separation of hydrostatic stress between type I and type II RA becomes smaller, which is likely due to a large fraction of type II RA under high hydrostatic stress in martensite matrix already transformed as strain increased to 5%.

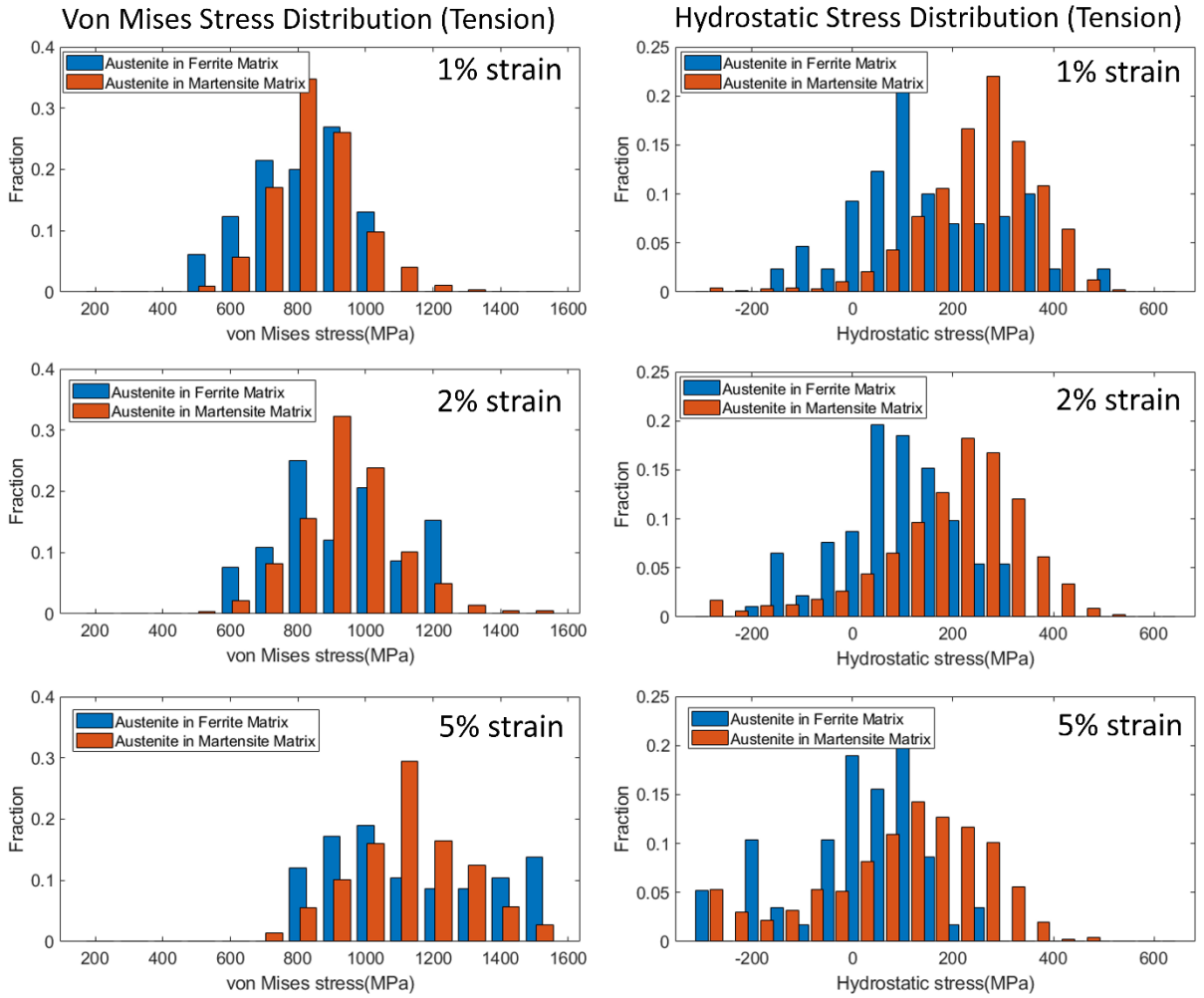


Fig. 19.

We also note that the von Mises stress and hydrostatic stress of bulk RA in all types matrix do not show a clear correlation, as shown in Figure 21, where each point corresponds to a bulk RA element at a location based on its stress state. The RA element under a high hydrostatic stress does not necessarily undertake a high or low von Mises stress.

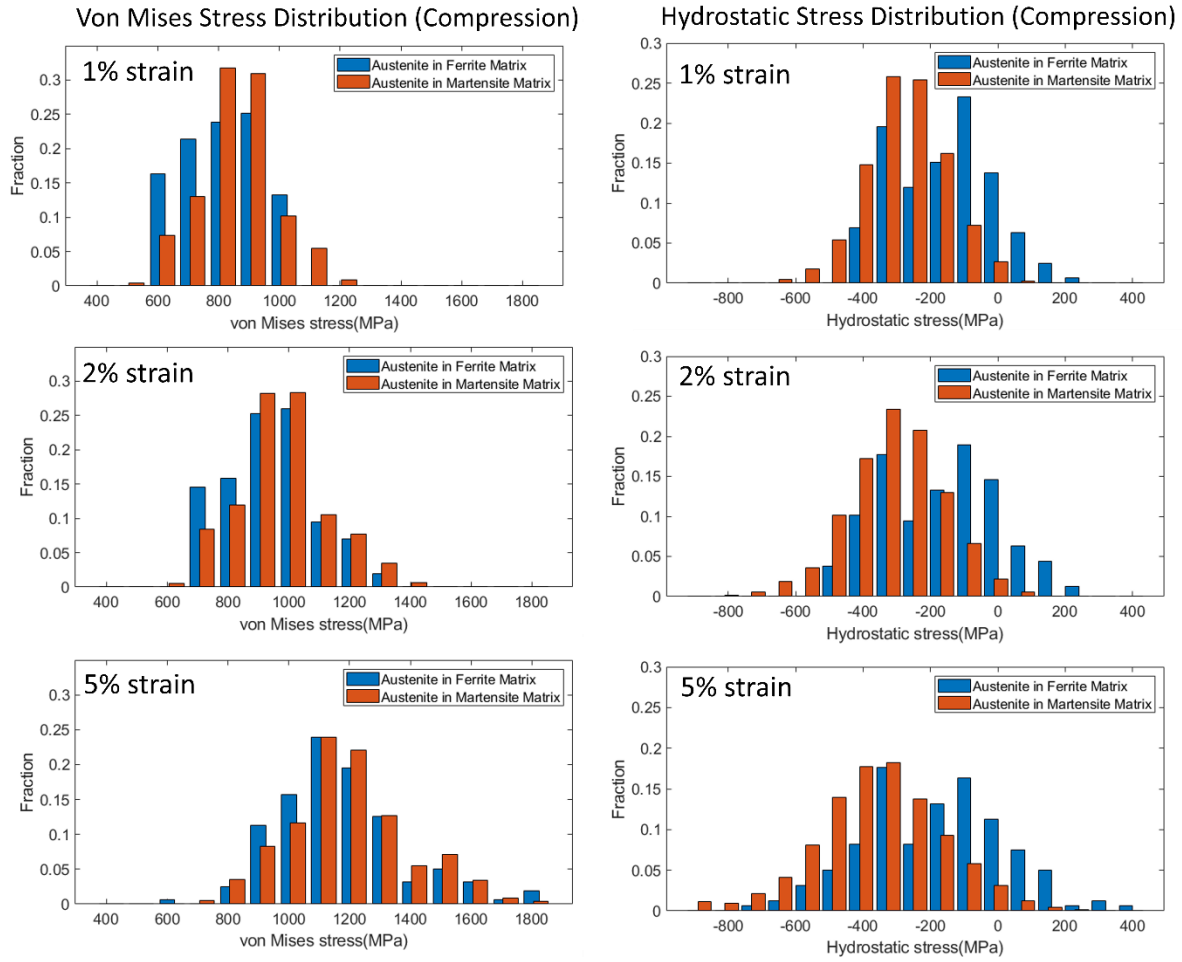


Fig. 20.

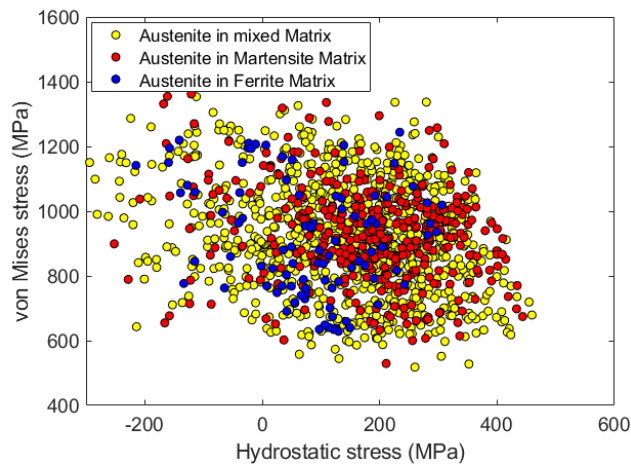


Fig. 21.

Connecting the observations in section 4.3 and 4.4, we make the following informed speculations:

1. The QP980 exhibits quite some tension-compression asymmetry in the stress-strain behavior, which is due to the different martensitic transformation rate of RA. The transformation rate is highly influenced by the local RA's stress-state. Using von Mises and hydrostatic stress invariants are simple yet effective metrics to characterize the stress-state relation to transformation of RA.

2. The local hydrostatic stress, which is quite heterogeneous in the QP980 microstructure, plays a critical role in martensitic transformation. Tensile hydrostatic stress promotes the martensitic transformation as it increases the mechanical energy for the transformation, and vice versa, the compressive hydrostatic stress inhibits the transformation.

3. The local hydrostatic stress state of RA depends significantly on the surrounding matrix. The ferrite matrix tends to transmit lower magnitude hydrostatic stress to the RA, while the martensite matrix leads to a higher magnitude of hydrostatic stress. This 'shielding' effect of ferrite matrix reduces the difference in the transformation rate under tension versus under compression loading, and thus reduces the tension-compression asymmetry of QP980. That is, if a microstructure is fabricated with lower volume fraction of ferrite phase, it is expected to show a higher level of martensitic transformation rate and tension-compression asymmetry.

4.4. Conduct large sets of crystal plasticity modeling using HPC and validation to predict austenite transformation kinetics in different deformation modes for the two selected grades.

4.4.1 Model descriptions

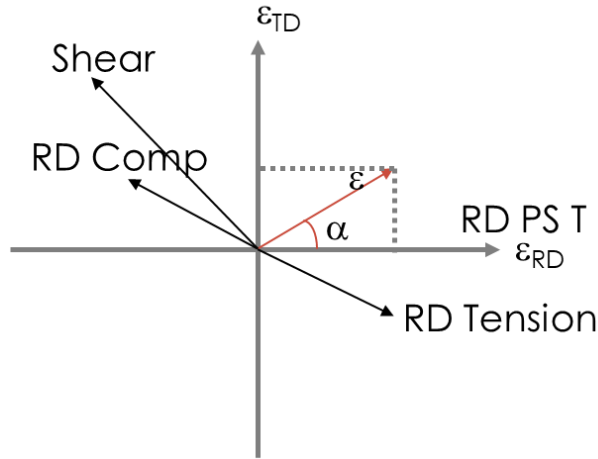
To construct a reduce order model for martensitic transformations, a large number of simulations are performed of a large number of strain paths. Since during stamping of steel sheet, a plane stress can reasonably be assumed, therefore we only consider strains on the steel sheet plane parallel to the surface, i.e the plane of rolling direction (RD) × transverse direction (TD). Fig. 22 is a explanatory sketch of strains paths: a general strain path has a length of ε and angle α with RD (the red vector in the figure).

With the assumption of non-compressibility during plastic deformation and the fact that the elastic deformation is considerably lower than that of the plastic strain, the equivalent strain of such a strain path can be expressed in the equation (28),

$$\bar{\varepsilon} = \left(\frac{2}{3} (2 + \sin 2\alpha) \right)^{\frac{1}{2}} \cdot \varepsilon \quad (28)$$

When $\alpha=0^\circ$, 45° or 135° , it is plane strain (PS) tension along RD, biaxial stretching and shear deformation (Fig. 28). The uniaxial tension and compression has $\alpha=33.5^\circ$ and 153.5° respectively (Fig. 28).

In this project, utilizing the developed CPFEM UMAT, we performed 26 simulations including strain paths of $\alpha=0$ to 345° with an interval of 15° and uniaxial tension and compression by the use of microstructure and unit-cell model as described in the previous sections.



Planar Strain Paths

Fig. 22. Sketch of planar (RD×TD) strain paths (deformation modes) in the RD×TD plane of a steel sheet. The red vector represent a strain path with a value of ϵ and an angle α with respect to rolling direction (RD). TD is the transverse direction. Several typical strain paths are along illustrated here: RD PS T, RD Tension and RD Compression represents plane strain tension, tension and compression along RD, respectively.

4.4.2 Results

The simulation results of the model of different strain paths are as shown in Figure 23 in terms of retained austenite volume fraction in percentage as a function of strain (ϵ). The figure is then changed into a relative new martensite (f^{α}/f_0^{α}) volume fraction as a function of equivalent strain (ϵ_{VM}) as in Figure 24. With $f^{\alpha} = f_0^{\alpha} - f^l$. As can be seen from the figure, the transformation is fastest when the strain path lies in the 1st quadrant of figure 22, i.e. $\alpha=0-90^{\circ}$, since it is in biaxial stretching region. The transformation is in the 3rd quadrant ($\alpha=180-270^{\circ}$) is in biaxial compression. The transformation is intermediate in quadrant 2 and 4 (green and blue curves in Fig. 24) where ϵ_{RD} and ϵ_{TD} has the opposite signs.

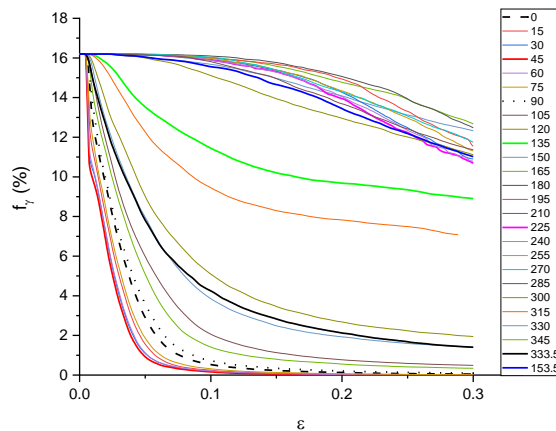


Fig. 23. The volume fraction in percentage as a function of strain vector (ϵ) for different strain paths in terms of angle α in Fig. 22.

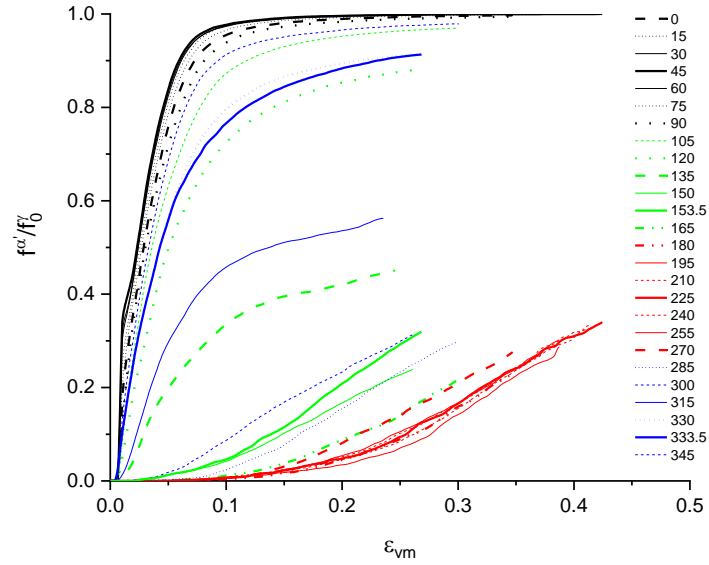


Fig. 24. The relative volume fraction of new martensite as a function of equivalent von Mises strain (ϵ_{vm}) for different strain paths in terms of angle α in Fig. 22, with the black curves representing the strain path of the 1st quadrant ($\alpha=0-90^\circ$), green curves in 2nd quadrant, red curve in the 3rd and the blue curve in the 4th.

A one element model (see Fig. 25) has been performed to obtain the relationship between strain path and triaxiality and the results are plotted in Fig. 26.

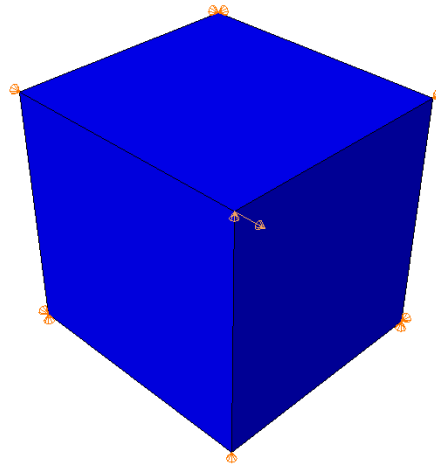


Fig. 25. The one element model

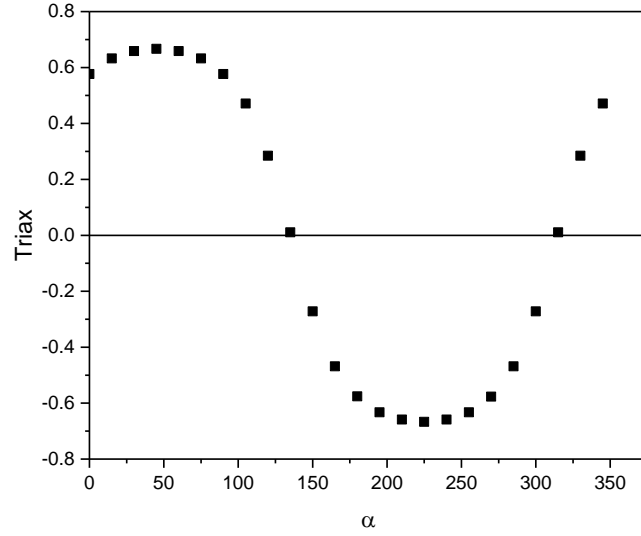


Fig. 26. The triaxiality as a function of strain paths angles (α)

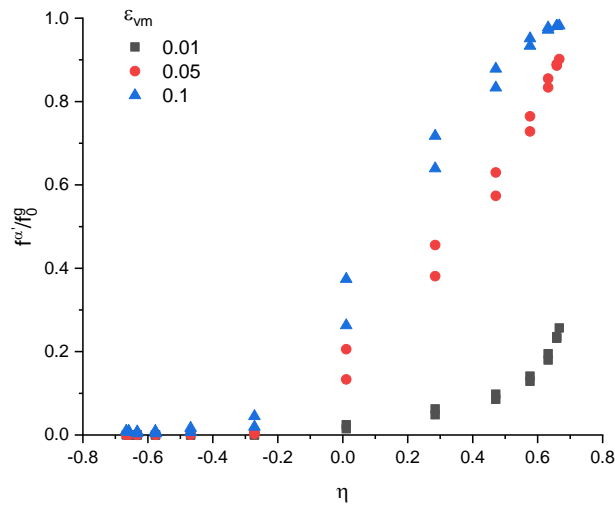


Fig. 27. The relative volume fraction of new martensite as a function of triaxiality for different equivalent strains

Using this information from Fig. 26 and the results from Fig. 24, the relative volume fraction of new martensite is obtained for different equivalent strain levels as shown in Fig. 27 and it is apparent that the transformed martensite is higher with increasing stress triaxiality.

4.5 Build RO-SVM for component level simulation and process parameter optimization

4.5.1 The RO-SVM model

As studied in many literatures, the martensitic transformation from austenite depends on the deformation mode or strain paths. It is well documented that there will have more transformation when the material is subject to tension than compression, due to effect that there is a volume expansion because of the transformation. The Olson-Cohen model is most well-known for calculating the normalized new transformed martensite,

$$\bar{f}\alpha' = 1 - e^{-\beta(1-e^{-\alpha\epsilon})^n} \quad (29)$$

Using this equation, it is found that the transformation kinetics can well fitted by using $n=1.6$ for the positive triaxiality cases (Fig. 28(a)), while $n=4$ with negative triaxiality cases (Fig. 28(b)). The fitted parameters are as shown in Table 1

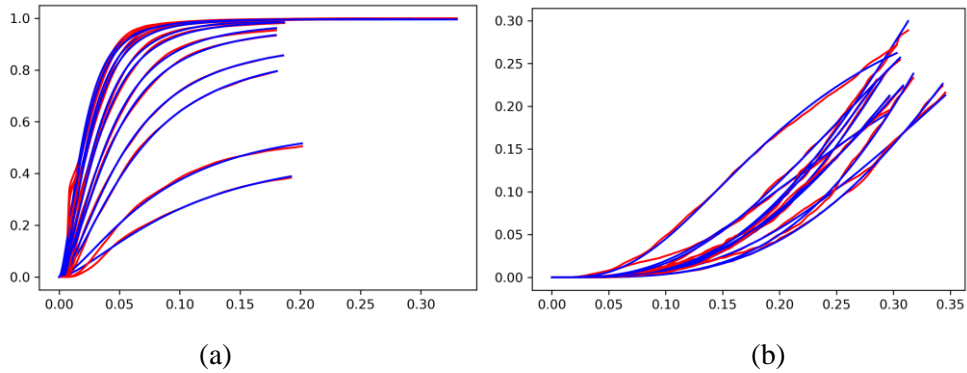


Fig. 28 The curve fitting with (a) $n=1.6$ for cases of positive η and (b) $n=4$ for cases of negative η .

Table 1 The fitted parameters with the Olsen-Cohen model

| Angle α | η | α | β | n |
|----------------|---------|----------|-----------|-----|
| 0 | 0.5767 | 10.71213 | 5.91555 | 1.6 |
| 15 | 0.6323 | 12.98717 | 6.30035 | 1.6 |
| 30 | 0.6588 | 16.01301 | 5.71799 | 1.6 |
| 45 | 0.6667 | 17.74801 | 5.4224 | 1.6 |
| 60 | 0.6588 | 15.79547 | 5.72137 | 1.6 |
| 75 | 0.6323 | 12.36474 | 6.19613 | 1.6 |
| 90 | 0.5767 | 10.89101 | 5.22476 | 1.6 |
| 105 | 0.4711 | 10.56613 | 3.54664 | 1.6 |
| 120 | 0.2845 | 10.11499 | 2.10277 | 1.6 |
| 135 | 0.01086 | 10.06571 | 0.63176 | 1.6 |
| 315 | 0.01086 | 11.63979 | 0.8534 | 1.6 |
| 330 | 0.2845 | 10.92203 | 2.43038 | 1.6 |
| 345 | 0.4711 | 10.21052 | 4.30858 | 1.6 |
| 150 | -0.2718 | 6.22626 | 0.42576 | 4 |
| 165 | -0.4683 | 3.13839 | 1.24758 | 4 |
| 180 | -0.5759 | 1.52355 | 9.33575 | 4 |
| 195 | -0.6327 | 0.79697 | 108.98207 | 4 |
| 210 | -0.6589 | 1.81916 | 9.38539 | 4 |
| 225 | -0.6667 | 2.41042 | 4.52809 | 4 |
| 240 | -0.6589 | 2.59221 | 3.49094 | 4 |
| 255 | -0.6327 | 2.74739 | 2.47867 | 4 |
| 270 | -0.5769 | 3.22086 | 1.61529 | 4 |
| 285 | -0.4683 | 4.5707 | 0.92462 | 4 |
| 300 | -0.2718 | 8.63815 | 0.41197 | 4 |

The fitted parameters are also plotted as a function of stress triaxiality in Fig. 26 (a) and (b) for positive triaxiality and negative triaxiality. For positive η , α parameter almost kept constant around 10.6 when $\eta < 0.6$, while it increases rapidly afterwards. β parameter increases quadratically, and after curve fitting, the following equation is obtained,

$$\beta = 0.64311 + 4.5252\eta + 5.57354\eta^2, \eta \geq 0 \quad (30)$$

For negative η , α and β parameters changes with η can be fitted as,

$$\alpha = 10.4434 + 12.4528\eta \quad (31)$$

$$\beta = 0.65181 - 9.777 \cdot 10^{-5} \cdot (1.4575 \cdot 10^{-7})\eta \quad (32)$$

or

$$\beta = 0.32416 \cdot (\eta + 0.69351)^{-0.72222} \quad (33)$$

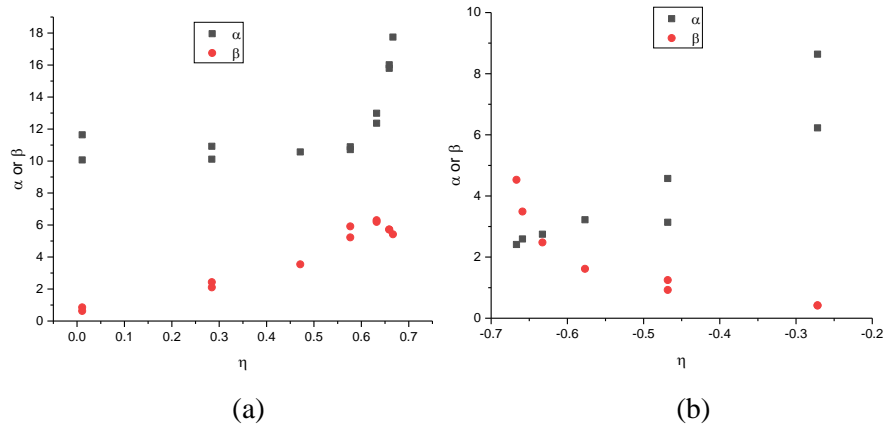


Fig. 29. The curve fitting parameters with (a) $n=1.6$ for cases of positive η and (b) $n=4$ for cases of negative η .

The equations of Olson-Cohen (OC) model (see equation (29)) and the relationship between OC model parameters and stress triaxiality through equations (30)-(33) can be used as reduced order model (ROM) and implemented in Abaqus/Explicit user material subroutine (VUMAT) for component level calculations.

4.5.2 Component level simulations

Three-point V-bending is selected for component level simulations and geometrical sketch is shown in Fig. 30(a). A 2D plane strain finite element model has been construct (Fig. 30(b)) with the use of the after-mentioned SV-ROM VUMAT will be used to represent the materials to be bent,

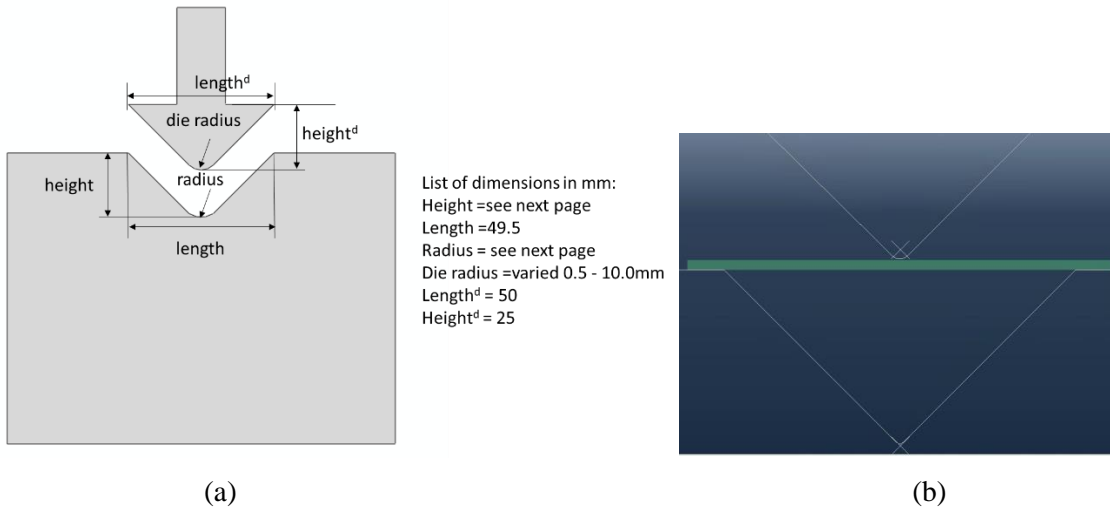


Fig. 30 The 3-Point V-bending geometry (a) and finite element model (b)

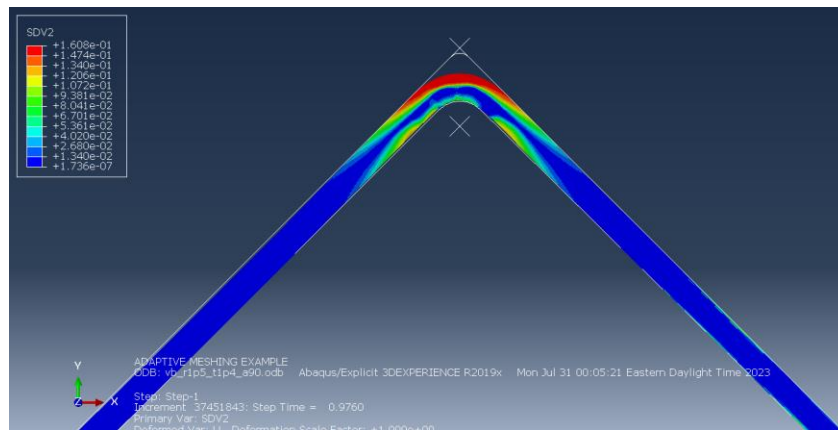


Fig. 31 The simulated new martensite volume fraction at the end of the bend deformation.

The simulation is performed on the FF980 steel which has 0.162 initial retained austenite volume fraction. The calculated results of new martensite volume fraction (NMVF) at the bend angle of 90° are as shown in Fig. 31. The evolutions with punch displacement (d) of the NMVF at the centerline elements of the bend are as shown the Fig. 32.

The retained austenite volume fraction (RAVF) can also be calculated by subtracting the NMVF from the initial austenite volume fraction and the distribution along the centerline can be shown in Fig. 33. Point 1 is at the top of tension side of the bend and point 70 is at the bottom of compression side bend. It can be seen that the volume fraction is reduced faster on the tension side than the compression side.

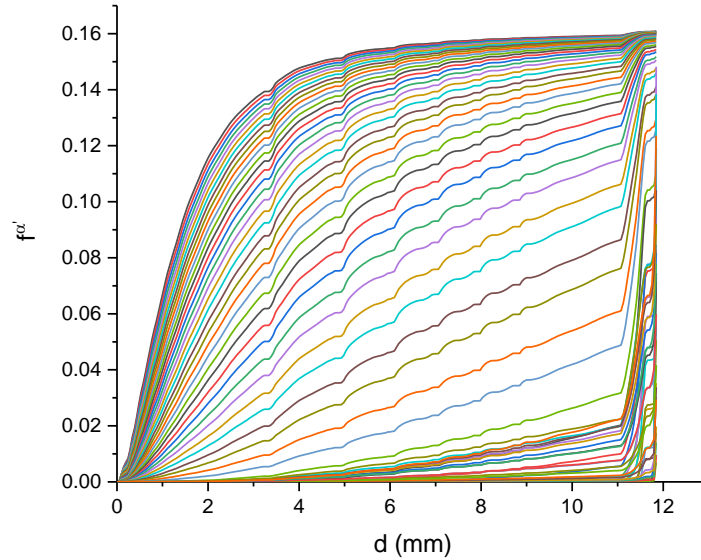


Fig. 32. The evolution of the calculated volume fraction of new martensite volume fraction with punch displacement at the center line of the bend.

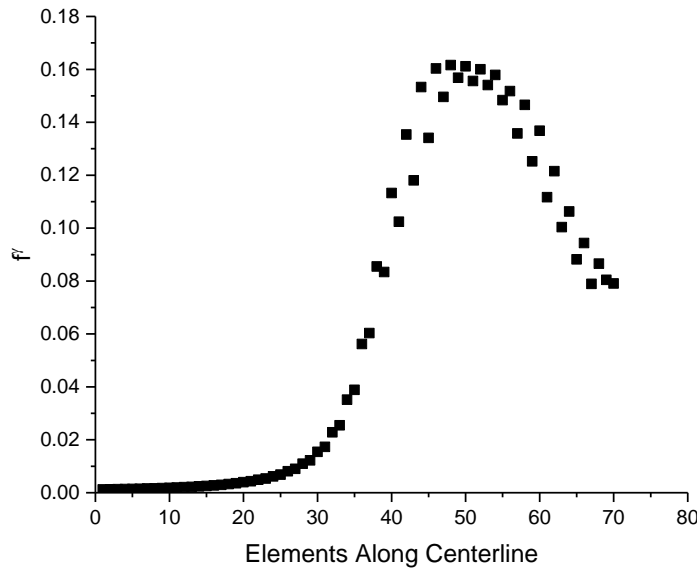


Fig. 33. The retained austenite volume fraction along the centerline of the bend.

5.0 Subject Inventions

No subject inventions were created as part of this CRADA.

6.0 Commercialization Possibilities

ArcelorMittal company appreciate the support from Department of Energy, advanced manufacturing office for supporting this project. This project fostered a new connection between the ArcelorMittal Company and Oak Ridge National Laboratory Energy & Manufacturing Science Division. The Oak Ridge National Laboratory team provided outstanding technical expertise and value to ArcelorMittal during this program.

ArcelorMittal and Oak Ridge teams will continue work on commercialization of the developed crystal plasticity model and state variable reduced order model software package.

7.0 Plans for Future Collaboration

In the near term, ArcelorMittal and Oak Ridge would like to submit a phase 2 proposal which will utilize the developed model to understand the fracture and damage mechanism and the formability of the studied 3rd gen advanced high strength steels.

8.0 Conclusions

A high-fidelity state of the art crystal plasticity finite element software has been developed at Oak Ridge National Laboratory for the prediction of transformation induced plasticity (TRIP) which is applicable to (third generation) advanced high strength steel which relies on the deformation induced retained austenite to martensitic transformation to provide both superior strength and ductility in the material, so that we can make thinner gauge material to suffice vehicle light-weighting. For the first time, the developed model considers the volume change during phase transformation and directly treat the transformation from bulky austenite to martensite, including volume, phase, and orientation changes. In the meantime, the phase transformation of the much finer film austenite is using a pseudo-slip approach. *In-situ* High energy X-ray diffraction (HEXRD) test has been used to calibrate the constitutive behaviors of the different phases in two of the third-generation advanced high strength steels (3GAHSS) in terms of slip system parameters and transformation model parameters.

Utilizing the developed & parameter calibrated crystal plasticity finite element model, a large number of unit-cell simulations were performed to cover different strain paths and stress-triaxiality states. The simulated results of martensitic transformation are then used to generate a state variable reduced order model (SV-ROM) and embedded in an user material subroutine for Abaqus. The SV-ROM has been applied to model 3-point V-bending of the 3GAHSS and austenite volume fraction has been successfully predicted from their comparison with high energy X-ray measurements.

9.0 References

- [1] J. Wu, P.J. Wray, C.I. Garcia, M. Hua, A.J. Deardo, Image quality analysis: A new method of characterizing microstructures, *ISIJ Int.* 45 (2005). <https://doi.org/10.2355/isijinternational.45.254>.
- [2] L. Ryde, Application of EBSD to analysis of microstructures in commercial steels, *Mater. Sci. Technol.* 22 (2006). <https://doi.org/10.1179/174328406X130948>.
- [3] Z. Feng, R. Pokharel, S.C. Vogel, R.A. Lebensohn, D. Pagan, E. Zepeda-Alarcon, B. Clausen, R. Martinez, G.T. Gray, M. Knezevic, Crystal plasticity modeling of strain-induced martensitic transformations to predict strain rate and temperature sensitive behavior of 304 L steels: Applications to tension, compression, torsion, and impact, *Int. J. Plast.* 156 (2022). <https://doi.org/10.1016/j.ijplas.2022.103367>.
- [4] R. Hielscher, T. Nyysönen, F. Niessen, A.A. Gazder, The variant graph approach to improved parent grain reconstruction, *Materialia*. 22 (2022). <https://doi.org/10.1016/j.mtla.2022.101399>.
- [5] F. Niessen, T. Nyysönen, A.A. Gazder, R. Hielscher, Parent grain reconstruction from partially or fully transformed microstructures in MTEX, *J. Appl. Crystallogr.* 55 (2022) 180–194. <https://doi.org/10.1107/S1600576721011560>.
- [6] J. Cheng, R. Lane, M. Kesler, J. Brechtel, X. Hu, R. Mirzaeifar, O. Rios, A.M. Momen, K. Nawaza, Experiment and Non-Local Crystal Plasticity Finite Element Study of Nanoindentation on Al-8Ce-10Mg Alloy, *Int. J. Solids Struct.* 233 (2021) 111233.
- [7] A.K. Behera, G.B. Olson, Prediction of Carbon Partitioning and Austenite Stability via Non-equilibrium Thermodynamics in Quench and Partition (Q&P) Steel, *JOM*. 71 (2019). <https://doi.org/10.1007/s11837-019-03369-z>.

- [8] A. Kozłowska, A. Grajcar, J. Opara, J. Kaczmarczyk, A. Janik, K. Radwański, Mechanical behaviour and micromechanical modelling of medium-Mn steel microstructure evolution, *Int. J. Mech. Sci.* 220 (2022). <https://doi.org/10.1016/j.ijmecsci.2022.107151>.
- [9] J. Gong, Predictive Process Optimization for Fracture Ductility in Automotive TRIP Steels, ProQuest Diss. Theses. (2013) 211. https://www.proquest.com/dissertations-theses/predictive-process-optimization-fracture/docview/1328167630/se-2?accountid=14512%0Ahttp://ucelinks.cdlib.org:8888/sfx_local?url_ver=Z39.88-2004&rft_val_fmt=info:ofi/fmt:kev:mtx:dissertation&genre=dissertations.
- [10] J.O. Andersson, T. Helander, L. Höglund, P. Shi, B. Sundman, Thermo-Calc & DICTRA, computational tools for materials science, *Calphad Comput. Coupling Phase Diagrams Thermochem.* 26 (2002). [https://doi.org/10.1016/S0364-5916\(02\)00037-8](https://doi.org/10.1016/S0364-5916(02)00037-8).
- [11] G.N. Haidemenopoulos, G.B. Olson, M. Cohen, K. Tsuzaki, Transformation plasticity of retained austenite in stage-I tempered martensitic steels, *Scr. Metall.* 23 (1989). [https://doi.org/10.1016/0036-9748\(89\)90412-2](https://doi.org/10.1016/0036-9748(89)90412-2).
- [12] X.C. Xiong, B. Chen, M.X. Huang, J.F. Wang, L. Wang, The effect of morphology on the stability of retained austenite in a quenched and partitioned steel, *Scr. Mater.* 68 (2013) 321–324. <https://doi.org/10.1016/j.scriptamat.2012.11.003>.
- [13] M.G. Lee, S.J. Kim, H.N. Han, Crystal plasticity finite element modeling of mechanically induced martensitic transformation (MIMT) in metastable austenite, *Int. J. Plast.* 26 (2010) 688–710. <https://doi.org/10.1016/j.ijplas.2009.10.001>.
- [14] H. Ledbetter, M. Dunn, Predicted habit planes from two models: Invariant-plane-strain and elastic-energy-minimization, in: *Proc. 1996 Int. Conf. Displac. Phase Transform. Their Appl. Mater. Eng.*, 1998.
- [15] J.M. Ball, R.D. James, Fine phase mixtures as minimizers of energy, *Arch. Ration. Mech. Anal.* 100 (1987). <https://doi.org/10.1007/BF00281246>.
- [16] K.F. Hane, T.W. Shield, Symmetry and microstructure in martensites, *Philos. Mag. A Phys. Condens. Matter, Struct. Defects Mech. Prop.* 78 (1998). <https://doi.org/10.1080/01418619808239984>.
- [17] D.S. Connolly, C.P. Kohar, W. Muhammad, L.G. Hector, R.K. Mishra, K. Inal, A coupled thermomechanical crystal plasticity model applied to Quenched and Partitioned steel, *Int. J. Plast.* 133 (2020) 102757. <https://doi.org/10.1016/j.ijplas.2020.102757>.
- [18] D.S. Connolly, C.P. Kohar, K. Inal, A novel crystal plasticity model incorporating transformation induced plasticity for a wide range of strain rates and temperatures, *Int. J. Plast.* 152 (2022) 103188. <https://doi.org/10.1016/j.ijplas.2021.103188>.
- [19] A.S.J. Suiker, S. Turteltaub, Computational modelling of plasticity induced by martensitic phase transformations, *Int. J. Numer. Methods Eng.* 63 (2005). <https://doi.org/10.1002/nme.1327>.
- [20] S. Turteltaub, A.S.J. Suiker, A multiscale thermomechanical model for cubic to tetragonal martensitic phase transformations, *Int. J. Solids Struct.* 43 (2006). <https://doi.org/10.1016/j.ijsolstr.2005.06.065>.
- [21] T. Park, L.G. Hector, X. Hu, F. Abu-Farha, M.R. Fellingner, H. Kim, R. Esmaeilpour, F. Pourboghraat, Crystal plasticity modeling of 3rd generation multi-phase AHSS with martensitic transformation, *Int. J. Plast.* 120 (2019). <https://doi.org/10.1016/j.ijplas.2019.03.010>.
- [22] J. Min, L.G. Hector, L. Zhang, J. Lin, J.E. Carsley, L. Sun, Elevated-temperature mechanical stability and transformation behavior of retained austenite in a quenching and partitioning steel, *Mater. Sci. Eng. A.* 673 (2016) 423–429. <https://doi.org/10.1016/j.msea.2016.07.090>.
- [23] S. Turteltaub, A.S.J. Suiker, Transformation-induced plasticity in ferrous alloys, *J. Mech. Phys. Solids.* 53 (2005). <https://doi.org/10.1016/j.jmps.2005.03.004>.
- [24] S. Ghosh, D. Dimiduk, Computational methods for microstructure-property relationships, 2011. <https://doi.org/10.1007/978-1-4419-0643-4>.
- [25] M. Groeber, S. Ghosh, M.D. Uchic, D.M. Dimiduk, A framework for automated analysis and simulation of 3D polycrystalline microstructures. Part 1: Statistical characterization, *Acta Mater.*

- 56 (2008) 1257–1273. <https://doi.org/10.1016/j.actamat.2007.11.041>.
- [26] M.A. Groeber, M.A. Jackson, DREAM.3D: A Digital Representation Environment for the Analysis of Microstructure in 3D, *Integr. Mater. Manuf. Innov.* 3 (2014) 56–72. <https://doi.org/10.1186/2193-9772-3-5>.
- [27] J. Cheng, X. Hu, H. Jong Bong, S. Ghosh, X. Sun, A finite element formulation for deformation twinning induced strain localization in polycrystal magnesium alloys, *Comput. Mater. Sci.* 190 (2021). <https://doi.org/10.1016/j.commatsci.2021.110323>.
- [28] X.H. Hu, X. Sun, L.G. Hector, Y. Ren, Individual phase constitutive properties of a TRIP-assisted QP980 steel from a combined synchrotron X-ray diffraction and crystal plasticity approach, *Acta Mater.* 132 (2017) 230–244. <https://doi.org/10.1016/j.actamat.2017.04.028>.
- [29] H.J. Bong, X. Hu, X. Sun, Y. Ren, Mechanism-based constitutive modeling of ZEK100 magnesium alloy with crystal plasticity and in-situ HEXRD experiment, *Int. J. Plast.* 113 (2019) 35–51. <https://doi.org/10.1016/j.ijplas.2018.09.005>.
- [30] Z. Feng, M. Zecevic, M. Knezevic, Stress-assisted ($\gamma \rightarrow \alpha'$) and strain-induced ($\gamma \rightarrow \epsilon \rightarrow \alpha'$) phase transformation kinetics laws implemented in a crystal plasticity model for predicting strain path sensitive deformation of austenitic steels, *Int. J. Plast.* 136 (2021) 102807. <https://doi.org/10.1016/j.ijplas.2020.102807>.
- [31] J. Cheng, M. Gussev, J. Allen, X. Hu, A.R. Moustafa, D.A. Splitter, A. Shyam, Deformation and failure of PrintCast A356/316 L composites: Digital image correlation and finite element modeling, *Mater. Des.* 195 (2020) 109061. <https://doi.org/10.1016/j.matdes.2020.109061>.
- [32] J. Kang, N.S. Pottore, H. Zhu, C.C. Tasan, An in situ investigation of neighborhood effects in a ferrite-containing quenching and partitioning steel: Mechanical stability, strain partitioning, and damage, *Acta Mater.* 254 (2023) 118985. <https://doi.org/10.1016/j.actamat.2023.118985>.